

# Increasing precipitation due to climate change could partially offset the impact of warming on glacier loss in the monsoon-influenced Himalaya until 2100 CE

Anya M. Schlich-Davies<sup>1\*</sup>, Ann V. Rowan<sup>2\*</sup>, Andrew N. Ross<sup>1</sup>, Duncan J. Quincey<sup>3</sup>, Vivi K. Pedersen<sup>4</sup>

<sup>1</sup>Priestley International Centre for Climate, School of Earth and Environment, University of Leeds, UK

<sup>2</sup>Department of Earth Science, University of Bergen and Bjerknes Centre for Climate Research, Bergen, Norway

<sup>3</sup>School of Geography, University of Leeds, UK

<sup>4</sup>Department of Geoscience, Aarhus University, Aarhus C, Denmark

\*These authors contributed equally to this work

Correspondence to: Ann V. Rowan ([ann.rowan@uib.no](mailto:ann.rowan@uib.no))

**Abstract.** Glacier mass in the Himalaya is projected to shrink by 53–70% due to climate change by 2100 CE. However, the impact of changes in precipitation amount and distribution on future glacier change remains uncertain because these variables are not often represented in glacier model projections. We explored the combined effects of past and future changes in air temperature and precipitation amount and distribution on the evolution of Khumbu Glacier in the Everest region of Nepal. We used a glacier modelling approach that forced an ice-dynamical glacier evolution model with surface mass balance calculations that included mesoscale meteorological variables derived from statistical downscaling of existing regional climate projections. Our simulations show that historical warming has committed Khumbu Glacier to mass loss of 10–23% during this century, and that under an intermediate future emissions scenario (RCP4.5), this glacier could lose 70% mass by 2100 CE due to warming. The projected increase in precipitation in tandem with warming could offset about half of the projected glacier loss, such that the total decrease in glacier mass by 2100 CE compared to the present day would be reduced to 34%. However, under a higher future emissions scenario (RCP8.5) glacier loss due to warming will not be compensated by changes in precipitation, but will instead result in substantial ablation above 6,000 m elevation, with devastating consequences for one of the highest glaciers on Earth.

## 1. Introduction

Projecting glacier change in response to climate change is important for determining the impact of anthropogenic warming on regional water availability (Pritchard, 2019). High Mountain Asia is projected to lose  $34 \pm 19\%$  of glacier mass by 2100 CE if warming is limited to  $1.5^\circ\text{C}$  to meet the ambitious Paris Agreement target (Kraaijenbrink et al., 2017). Less ambitious projections give  $53 \pm 23\%$  glacier mass loss by 2100 CE under the intermediate emissions scenario RCP4.5, and  $69 \pm 20\%$  under the high emissions scenario RCP8.5 (Kraaijenbrink et al., 2017; Marzeion et al., 2020; Rounce et al., 2023). Such projections are challenging to make, because accumulation and ablation processes in mountain environments are driven by orographic feedbacks between high-relief topography and atmospheric circulation systems such as the South Asian Summer Monsoon (e.g., Bookhagen and Burbank, 2006). Furthermore, large uncertainties arise from the challenge of simulating the interactions between the mass balance regimes of monsoon-influenced glaciers, where accumulation and ablation both occur during the monsoon season, and the dynamics of glaciers flowing through high-relief topography that includes processes such as the development of supraglacial debris layers that modify surface melting (Dehecq et al., 2019; Miles et al., 2018b; Salerno et al., 2023). Variability in the extent and intensity of the Indian Summer Monsoon during the Last Glacial Maximum was shown to affect glacier expansion in the monsoon-influenced Himalaya through changes in snowfall distribution (Benn

54 and Owen, 1998; Owen et al., 2009). Future Indian Summer Monsoon precipitation and variability  
55 projected in Global Circulation Models (GCMs) will increase with current global warming  
56 (Katzenberger et al., 2021), but as yet, the effect of projected changes in precipitation amount, timing,  
57 and phase (rain/snow) on Himalayan glaciers remain poorly constrained (Immerzeel et al., 2012; Mölg  
58 et al., 2014; Ragetti et al., 2016; Shaw et al., 2022; Shea et al., 2015).

59  
60 Supraglacial debris covers 4–7% of glacier surfaces globally and 30% of glacier ablation areas in the  
61 Himalaya, and modifies the response of glaciers to climate change relative to regional trends (Herreid  
62 and Pellicciotti, 2020; Kraaijenbrink et al., 2017; Rounce et al., 2023; Rowan et al., 2015). Satellite  
63 observations show that the rate of glacier mass loss across the Himalaya has accelerated over the last  
64 40 years for both clean-ice glaciers and debris-covered glaciers (Maurer et al., 2019). Observations and  
65 modelling studies indicate that thick supraglacial debris caused historical mass loss from debris-covered  
66 glaciers to lag that of clean-ice glaciers, such that debris-covered glaciers are currently larger than would  
67 otherwise be the case (King et al., 2020; Rounce et al., 2023; Rowan et al., 2021). However, the  
68 dampening effect of supraglacial debris on glacier mass loss is overturned by the development of  
69 extensive supraglacial ponds and ice cliffs within debris layers (Miles et al., 2018a; Strickland et al.,  
70 2023) and the stagnation and detachment of debris-covered tongues from the upper and more active  
71 sections of these glaciers (Rowan et al., 2021). Quantifying the impact of feedbacks set up by the  
72 formation and expansion of supraglacial debris layers at a regional scale requires exploring such  
73 processes at scales that can be resolved in ice-dynamical glacier evolution models (Rowan et al., 2015;  
74 Nicholson et al., 2021; Compagno et al., 2022). These processes can be considered in 2-D (along the  
75 glacier flowline) either considering stochastic debris delivery to the glacier (Vacco et al., 2010) or  
76 continuous debris delivery, which can result in the over-accumulation of debris at the terminus  
77 (Anderson and Anderson, 2016; Ferguson and Vieli, 2020; Juvet et al., 2011), or in 3-D (using the  
78 horizontal and vertical ice-flow fields), which simulates the lateral transport and deposition of debris to  
79 the margins of the ablation area (Rowan et al., 2015; Wirbel et al., 2018). While recent rapid warming  
80 has resulted in a rise in regional equilibrium line altitude (ELA) and caused recession and collapse of  
81 glacier termini for both clean-ice glaciers and debris-covered glaciers (King et al., 2020), the decay of  
82 the former ablation areas of debris-covered glaciers is delayed by supraglacial debris, such that the  
83 terminus of the actively flowing glacier can remain in contact with the stagnant former ice tongue rather  
84 than separating (Maurer et al., 2019; Pellicciotti et al., 2015; Rowan et al., 2021).

85  
86 In common with most large debris-covered Himalayan glaciers, Khumbu Glacier in the Everest region  
87 of Nepal (Fig. 1) is in greater imbalance with climate than a climatically equivalent clean-ice glacier,  
88 and has maintained a more extensive ice volume than would be possible without supraglacial debris  
89 (Rowan et al., 2021). Khumbu Glacier (RGI2000-v7.0-G-15-08331) is 16.0 km long with an area of  
90 26.4 km<sup>2</sup>. The median glacier elevation is 6,025 m a.s.l. from the terminus at 4,879 m a.s.l. to the  
91 headwall at 7,981 m a.s.l. (RGI 7.0 Consortium, 2023). The stagnant debris-covered tongue has an area  
92 of 6.2 km<sup>2</sup> (23% of the total glacier). As a result of reduced ice flux from the accumulation area, the  
93 debris-covered tongue no longer receives much (or any) input of ice, and has dynamically detached  
94 from the active glacier (Fig. 1C); this observation is confirmed by the rapid reduction in ice flow and  
95 the peak in glacier surface lowering below the Khumbu Icefall where the debris layer is thinnest (King  
96 et al., 2020; Quincey et al., 2009). Observations and modelling of the dynamics and structure show that  
97 the tongue for 5 km upglacier from the terminus (25% of the total length, 20% of total ice volume) is  
98 stagnant and dynamically detached from the active glacier in the last century (Miles et al., 2022;  
99 Quincey et al., 2009; Rowan et al., 2021). Basal ice at the glacier surface indicates that the active  
100 terminus overrides the stagnant glacier tongue (Miles et al., 2021) and measurements of surface  
101 displacement show no longitudinal flow through the detached debris-covered tongue, which is  
102 collapsing laterally at a rate of about 3 m a<sup>-1</sup> (Watson et al., 2017). Therefore, the active glacier and the  
103 stagnant debris-covered tongue evolve along different trajectories, and only the part of Khumbu Glacier  
104 above the terminus of the active glacier can be considered dynamic (Miles et al., 2022). Projections of  
105 future glacier evolution should therefore discount the heavily debris-covered former tongue, which is  
106 decaying *in situ* without any input of new ice from the accumulation area, while considering the  
107 development of supraglacial debris across the ablation area of the active glacier.

108

109 We applied a novel glacier modelling approach to Khumbu Glacier to test the hypothesis that changes  
110 in precipitation in response to climate change will reduce the impact of warming on glacier mass loss.  
111 Khumbu Glacier is a benchmark debris-covered glacier in the monsoon-influenced Himalaya flowing  
112 from 7,981 m above sea level (a.s.l.) to 4,879 m a.s.l. that is representative in terms of elevation of the  
113 majority of glaciers in the Central and Eastern Himalaya (Fig. 1B). The ‘Little Ice Age’ (LIA) maximum  
114 of Khumbu Glacier occurred about 200–500 years before present, which is consistent with ages  
115 produced for moraines elsewhere in the central Himalaya (Hornsey et al., 2022; Rowan, 2017). Khumbu  
116 Glacier was slightly larger than today during the late Holocene, transitioning from a clean-ice glacier  
117 with high velocities and efficient export of debris to a debris-covered glacier with lower velocities after  
118 the LIA; this change was initiated by the reduction in ice flux to the glacier tongue promoted by a rise  
119 in ELA (Rowan et al., 2015). We used a 3-D ice-flow model forced by mass balance calculated from  
120 mesoscale meteorological variables to simulate the evolution of Khumbu Glacier from the late  
121 Holocene (~1 ka) through the present day (2015 CE) until 2100 CE using results from three downscaled  
122 Regional Climate Models (RCMs) under two Relative Concentration Pathways (RCPs). This approach  
123 represents an advance in the use of such models to understand the evolution of Himalayan glaciers  
124 whereby mesoscale meteorological forcing of surface mass balance is used with a thermomechanical  
125 glacier model to represent the processes of sublimation, snow avalanching, and debris transport, all of  
126 which are important controls on the mass balance of Himalayan glaciers (Kneib et al., 2025).  
127 Simulations start from the late Holocene when Khumbu Glacier was last in dynamic equilibrium with  
128 the local climate, as evidenced by large ice-marginal moraines dated to  $1.3 \pm 0.1$  ka surrounding the  
129 present-day glacier (Hornsey et al., 2022), and when the glacier surface was free of debris (Rowan et  
130 al., 2015).

131

132

## 133 2. Methods

### 134 2.1 Glacier model experimental design

135 The glacier model experiments used mesoscale meteorological variables to calculate surface mass  
136 balance for the Khumbu Glacier catchment in combination with a debris-covered glacier evolution  
137 model to represent the surface processes that modify mass balance (Fig. 2A). Our approach produced a  
138 total of six simulations of Khumbu Glacier to 2100 CE from three CORDEX South Asia region RCMs  
139 (NOAA, CCCma, IPSL; Lutz et al., 2016) under two RCPs (RCP4.5 and RCP8.5; Collins et al., 2013)  
140 to explore the impacts of possible variability in future precipitation amount and distribution in tandem  
141 with warming on glacier evolution. Before we used the RCMs to force the future climate scenarios, we  
142 evaluated their capabilities against observations of present-day weather and climate. The experimental  
143 design represents an advance compared with previous glacier modelling efforts by including in each  
144 simulation; (1) mesoscale meteorological phenomena, including sublimation, (2) the redistribution of  
145 surface mass by snow avalanching, and (3) the feedbacks between debris transport, ice flow and mass  
146 balance. This section describes the experimental design for the glacier modelling workflow,  
147 downscaling of the present-day RCMs using meteorological data from automatic weather stations  
148 (AWS) in the Khumbu Valley, downscaling of the future RCMs for both RCPs, the surface energy and  
149 mass balance calculations using COSIPY (Sauter et al., 2020) and the debris-covered glacier evolution  
150 modelling using iSOSIA (Rowan et al., 2015). A reference simulation and sensitivity experiments were  
151 carried out for the period 2013–2015 CE, and the simulations of future glacier change represented the  
152 period 2015–2100 CE. Additional information about the development and testing of the modelling  
153 approach is provided in Appendix A.

154

155 The spin-up simulation from the ice-free model domain to represent the late Holocene glacier was  
156 forced using a simple approximation of mass balance. The ice-free model domain was found by  
157 subtracting the estimated ice thickness (Farinotti et al., 2019) from a 30-m digital elevation model  
158 (DEM) acquired from the Shuttle Radar Topography Mission (Farr et al., 2007). The ice-free model  
159 domain incorporated the full hydrological catchment including the steep hillslopes in the Western Cwm  
160 that provide snow to the glacier surface by avalanching. As a starting point for our transient simulations  
161 of Khumbu Glacier, we reconstructed the late Holocene glacier from the ice-free domain using an ELA  
162 of 5,325 m a.s.l. and an atmospheric lapse rate of  $-4.0^{\circ}\text{C km}^{-1}$  in a 5,000 year simulation. Accumulation  
163 above the ELA was calculated as a function of elevation  $0.2 \text{ mm m}^{-1}$  up to a maximum of 2.0 m water

164 equivalent (w.e.) per year and ablation was calculated as a function of elevation  $0.5 \text{ mm m}^{-1}$  up to a  
165 maximum of  $2.0 \text{ m w.e. a}^{-1}$ . This simulation continued through the LIA forced by a step change in mean  
166 annual air temperature (MAAT) equivalent to  $1.5^\circ\text{C}$  colder than the present day over 500 years  
167 following the approach of Rowan et al. (2015, 2021). Ice-marginal moraines denoting the late Holocene  
168 ( $1.3 \pm 0.1 \text{ ka}$ ) glacier extent and thickness (Hornsey et al., 2022) were used to constrain the spin-up  
169 simulation.

170  
171 The late Holocene simulation was forced to present-day (2015 CE) conditions using three surface mass  
172 balances (one from each RCM) calculated using the Coupled Snowpack and Ice-surface Energy and  
173 Mass Balance model in Python (COSIPY v1.3) (Sauter et al., 2020). These simulations were evaluated  
174 against a range of observations of present-day glaciology and previous glacier model experiments (Fig.  
175 3), and the experiment using the NOAA RCM was identified as the starting point for all future  
176 simulations because this was most representative of the observed glacier. We simulated only the active  
177 section of the glacier beyond 2015 CE and added the dynamically detached debris-covered tongue  
178 simulated at the present day to the model domain as a static topographic feature for the future  
179 simulations. The volume of the detached tongue was calculated by using the simulated present-day  
180 velocity field to separate the simulated present-day ice volume where velocities declined below  $10 \text{ m}$   
181  $\text{a}^{-1}$ . Thus, we arrived at the present-day from the LIA maximum simulation by forcing the LIA glacier  
182 with the 2015–2020 CE mass balance for 200 years.

183  
184 We used the output from the present-day simulation with the 2095–2100 CE mass balance calculated  
185 using COSIPY to force the model to 2100 CE over a period of 85 years. The glacier model simulations  
186 continued from the present day to 2100 CE forced by distributed glacier surface mass balances  
187 calculated for each of the three RCMs and two RCPs using COSIPY. The three RCMs and two future  
188 RCPs represented a range of possible future climates with distinctly different precipitation trends—  
189 equivalent to dry, moderate, and wet scenarios for warming of  $1.4\text{--}2.2^\circ\text{C}$  under RCP4.5 and  $3.8\text{--}4.1^\circ\text{C}$   
190 under RCP8.5 (Table 1; Fig. 2D; Section 2.3). We used time slices representing the present day (2015–  
191 2020 CE) and the end of the 21<sup>st</sup> Century (2095–2100 CE) to calculate surface mass balance, and the  
192 preceding decade was used to evaluate these time slices (see Section 3.3). We used this step forcing,  
193 whereby the future mass balance was imposed and the glacier adjusted to this from the start of the  
194 century in question, rather than interpolating mass balance over time to reduce the computational  
195 expense of the surface mass balance and glacier modelling ( $\sim 24$  hours per simulation).

196  
197 Estimates from a global glacier modelling study indicate that avalanching contributes up to 18% of  
198 regional accumulation to glaciers in the monsoon-influenced Himalaya (Kneib et al., 2025) and  
199 observations of high-elevation Himalayan glaciers, including Khumbu Glacier, suggest that up to 75%  
200 of accumulation occurs by avalanching rather than direct snowfall (Fig. 1D) (Benn and Lehmkuhl,  
201 2000; Laha et al., 2017). Avalanching affects mountain glaciers in two ways; (1) by moving snow from  
202 steep hillslopes onto the glacier surface thus increasing accumulation from that calculated from direct  
203 snowfall onto the glacier surface, and (2) by redistributing snow across steep sections of the glacier  
204 surface (Kneib et al., 2025). We examined the uncertainty in accumulation resulting from the application  
205 of a calculation in iSOSIA to move snowfall from slopes susceptible to avalanching (see Section 2.6).  
206 If avalanching was not considered in iSOSIA, then the accumulation of snow calculated using COSIPY  
207 within the catchment but outside of the glacier outline would have no impact on accumulation resulting  
208 in an underestimation of ice volume, and the steep sections of the glacier would hold more mass than  
209 expected. For example, when avalanching was not simulated and accumulation occurred at a uniform  
210 rate of  $2.0 \text{ w.e. m a}^{-1}$  across the Western Cwm accumulation area, Khumbu Glacier had a similar extent  
211 but a volume more than double that of the glacier simulated with avalanche redistribution of snow,  
212 because mass was not redistributed effectively across steep sections of the glacier surface (result not  
213 shown).

214

## 215 **2.2 Meteorological data collection and analysis**

216 The first meteorological observations for the Nepal Himalaya were collected during the 1970s and  
217 found a trend of diurnal precipitation on ridges and nocturnal precipitation in valley floors (Ageta, 1976)  
218 reflecting cloud development from orographic convection during the day. Continuously recording AWS

219 were first installed in the region in the 1990s at the Pyramid Observatory near Lobuche village, where  
220 Bollasina et al. (2002) analysed of the monsoon from meteorological observations collected between  
221 1994 and 1999, finding that the onset (decay) of the Indian Summer Monsoon was distinguished by  
222 higher (lower) daily precipitation totals, mean relative humidity and atmospheric pressure and a reduced  
223 (increased) diurnal range in atmospheric temperature. Bollasina et al. (2002) identified two daily  
224 profiles in precipitation and wind direction thought to be related to the monsoon. In addition, five-day  
225 and ten-day precipitation cycles were observed linked to oscillations in the Tibetan High. A new AWS  
226 was installed at the Pyramid Observatory at 5,035 m a.s.l. in September 2000 as part of a network in  
227 the Dudh Koshi valley of six AWS between 2,680 to 5,700 m a.s.l., in addition to some short-lived  
228 higher-elevation stations, maintained by the Ev-K2-CNR network. The Pyramid Observatory AWS  
229 included a snow depth sensor between 2009 and 2010, but the data were discontinuous and inconsistent,  
230 and the measurement period ended in December 2010. A second AWS was installed in the same location  
231 by the GlacioClim network in 2013 (Wagnon et al., 2013; Sherpa et al., 2017) provides a longer period  
232 of continuous data collection. More recently, a network of 5 AWS including the highest elevations in  
233 the Khumbu catchment were installed by the National Geographic project at Phortse (3,810 m a.s.l.),  
234 Everest Base Camp (5,315 m a.s.l.), Camp 2 (6,464 m a.s.l.), the South Col (7,945 m a.s.l.) and the  
235 Balcony (8,430 m a.s.l.) (Matthews et al., 2020). However, at time of writing, there are no continuous  
236 records of high-elevation meteorological variables that span a longer period than 15 years, making the  
237 calculation of climate normals impossible. In this study, we analysed data from these various sources  
238 for evaluation of mesoscale trends in the upper Khumbu Valley and for use to downscale RCMs and  
239 evaluate the results of our calculations. The location of the AWS is shown in Fig. 1C. Gaps in the air  
240 temperature and precipitation data were filled using interpolated data from neighbouring stations where  
241 required (as described in Appendix A).

242  
243 The AWS data were used to make a reference simulation in COSIPY of the surface energy fluxes and  
244 mass balance of the Khumbu Glacier catchment between 2013–2015 for model development and  
245 sensitivity experiments (Fig. 4 and Fig. 5). We compiled 14 years of meteorological observations from  
246 the two AWS provided by the GlacioClim network at the Pyramid Observatory (5,050 m a.s.l. and 5,035  
247 m a.s.l.) and the West Changri Nup Glacier AWS (5,363 m a.s.l.) (Wagnon et al., 2013; Sherpa et al.,  
248 2017). All meteorological data were collected for the period December 2010 to November 2019, apart  
249 from precipitation which was only recorded between December 2012 to November 2016. All  
250 meteorological data (excluding precipitation) used for the reference simulation were taken from the  
251 West Changri Nup AWS. Given the frequency of missing precipitation data from the AWS, the  
252 undercatch of snow associated with tipping bucket rain gauges, and the scarcity of high-elevation  
253 precipitation measurements, precipitation was not varied with elevation in the reference simulation.  
254 Precipitation data for the reference simulation were collected from the GlacioClim Geonor precipitation  
255 gauge at the Pyramid Observatory (5,035 m a.s.l.) because this precipitation gauge provides a longer  
256 period of continuous observations than the other gauges and avoids errors due to low precipitation  
257 amounts measured by tipping bucket gauges, which are known to systematically underestimate snowfall  
258 particularly during high winds (Sherpa et al., 2017). Precipitation was measured at 15-minute intervals  
259 using a Geonor T-200BM sensor mounted 1.8 m above the surface. Evaporation from the bucket was  
260 blocked by a layer of oil, but some loss did occur, as evidenced by precipitation values below 0 mm.  
261 Noise from wind and evaporation were corrected for by compensating any negative change over the  
262 15-minute time step with the neighbouring positive value such that accumulated precipitation was  
263 unchanged. Periods with prolonged evaporation were set to zero. Undercatch of snowfall by rainfall  
264 gauges was corrected through precipitation phase partitioning using wind speed observations (Wagnon  
265 et al., 2009). Air temperature was interpolated to match the height of the precipitation gauge using  
266 hourly lapse rates that averaged  $-5.89\text{ }^{\circ}\text{C km}^{-1}$ . COSIPY was run for both elevations using the non-  
267 adjusted temperature data for 5,336 m a.s.l. and the adjusted temperature data for 5,035 m a.s.l. and it  
268 made little impact on the model results. Simulated meteorological variables were evaluated at the  
269 highest elevations using the National Geographic AWS stations at Camp 2 (6,464 m a.s.l.) and the South  
270 Col (7,945 m a.s.l.) using data for May–November 2019 (Matthews et al., 2020).

271  
272 Direct solar radiation across the model domain was corrected for the slope, azimuth, and shadowing  
273 potential of each pixel (Wohlfahrt et al., 2016; Sauter et al., 2020). A footprint-weighted correction was

274 also applied to horizontal measurements of net radiation. The fraction of diffuse incoming shortwave  
275 radiation was estimated by using the ratio of total shortwave (global) radiation and potential shortwave  
276 radiation to define a clearness index (Wohlfahrt et al., 2016). This clearness index was used to calculate  
277 diffuse radiation, which was calibrated with data from the Neustift eddy covariance station in the  
278 Austrian Alps (Wohlfahrt et al., 2008). Pressure was distributed across the domain by first calculating  
279 sea-level pressure (*cf.* Lente and Osz, 2020) and then interpolated with the barometric equation. The  
280 relative humidity gradient was calculated as  $-0.002\% \text{ m}^{-1}$  using data from the Ev-K2-CNR and the  
281 GlacioClim AWS networks, and evaluated by comparison with measurements made by the National  
282 Geographic network AWS ranging in elevation from 3,810–8,430 m a.s.l. (Matthews et al., 2020) to  
283 capture trends at higher elevations. The distributed radiative fluxes were compared with the same high-  
284 elevation stations for 2019 to assess the efficacy of this method across the domain. Wind speed was  
285 assumed to be uniform across the domain.

286

### 287 **2.3 Present-day RCM downscaling using meteorological observations**

288 Six RCMs were assessed on their fidelity to present-day climate using hindcasting (Biemans et al.,  
289 2013) with an emphasis on temperature seasonality and seasonal precipitation dynamics given the  
290 importance of these variables for glacier mass balance. RCMs from the Coordinated Regional  
291 Downscaling Experiment (CORDEX) South Asia domain were dynamically downscaled from CMIP5  
292 GCMs by the Indian Institute of Tropical Meteorology to a 50 km spatial resolution (Lutz et al., 2016)  
293 and collected for the grid box containing Khumbu Glacier ( $27.9065056^\circ\text{N}$ ,  $86.4352951^\circ\text{E}$ ). Three of  
294 the six CORDEX South Asia RCMs (NOAA, CCCma, IPSL) spanning a range of possible future  
295 precipitation conditions (Table 1) were selected as discrete scenarios for the glacier surface energy and  
296 mass balance calculations. The three remaining RCMs were discounted due to being intermediate to  
297 those selected for our experiments (*i.e.* close to the future precipitation scenario represented by CCCma)  
298 or particularly poor at reproducing seasonal temperature and precipitation cycles. For example, despite  
299 the annual precipitation sums from the CSIRO RCM being closest to observed values and having the  
300 potential to be the ‘driest’ scenario examined, analysis of precipitation seasonality indicated that the  
301 monsoon signal was completely absent with this RCM instead showing a strong dominance of winter  
302 precipitation.

303

304 The present-day RCM results were downscaled using quantile mapping, also known as “distribution  
305 mapping”, using 14 years of observations collected between January 2006 and November 2019 from  
306 three AWS as described in Section 2.2. Parametric quantile mapping (Piani et al., 2010) was used to  
307 downscale the RCM to a daily time step at the resolution of the DEM, whereby a statistical relationship  
308 between the raw climate model outputs and observations was formed by substituting the RCM results  
309 with observations at a cumulative density function of the prescribed distribution (*e.g.*, a Gaussian  
310 distribution for temperature; Luo et al., 2018; a gamma distribution for precipitation; Piani et al., 2010).  
311 This correction was applied to the raw RCM outputs to produce a third downscaled dataset which had  
312 an improved the fit to the observations (Fig. 2C and 2D). The quantile mapping approach was chosen  
313 because this is effective for downscaling precipitation and reduces errors in the standard deviation, the  
314 coefficient of variation, and the skewness of distributed values relative to other methods (Lafon et al.,  
315 2013; Reiter et al., 2018). The AWS data were used to disaggregate the daily downscaled present-day  
316 and end-of-century climate model outputs to an hourly resolution for energy balance modelling. All  
317 meteorological variables, excluding precipitation, were downscaled using the MELODIST Python tool  
318 (Förster et al., 2016). Seasonal means were applied for precipitation to reproduce the ‘nocturnal peak’  
319 seen during the monsoon that MELODIST was unable to replicate (Figs. A1, A2 and A3). Further  
320 information on the meteorological data analysis and RCM downscaling are provided in Appendix A.

321

### 322 **2.4 Future RCM downscaling**

323 Two future emission scenarios (RCP4.5 and RCP8.5) were available from CORDEX South Asia, which  
324 represent intermediate and high emissions by 2100 CE relative to the present day. These two emissions  
325 scenarios are frequently used in climate impact studies enabling the comparison of our results with  
326 studies that use other climate/glacier model projections. The two future emissions scenarios were  
327 analysed for each of the three CORDEX RCMs to account for the inherently high uncertainties in future  
328 precipitation trends associated with climate models and the interplay of changing precipitation with

329 atmospheric warming. The same statistical downscaling approach and disaggregation used for the three  
330 present-day RCMs described in Section 2.3 was applied to the raw CORDEX RCM daily outputs for  
331 the three future RCM time slices under RCP4.5 and RCP8.5. The temperature change between the  
332 present day and the future time slices was preserved and there was no evidence of any imposed  
333 strengthening in the monsoon resulting from downscaling. An increase in the frequency of days per  
334 year outside of the monsoon season with high precipitation amounts (defined here as over 15 mm of  
335 daily precipitation) accounted in large part for the higher annual precipitation amounts relative to the  
336 present day that were found in four out of the six RCMs. However, the total future annual precipitation  
337 increase was on average 8.8% greater in the downscaled climates relative to the raw RCMs, suggesting  
338 that this positive trend was inflated by downscaling. The downscaled climates reduced the frequency  
339 of precipitation, although, as in present day observations, monsoon precipitation occurred frequently  
340 and could be characterised as predominantly drizzle in the future.

341

## 342 2.5 Surface energy balance modelling

343 COSIPY is a leading open-source method for estimating glacier surface mass balance and has  
344 previously been applied to glaciers in High Mountain Asia. COSIPY includes a calculation of  
345 sublimation, which is an important ablation process for high-elevation glaciers because ablation can  
346 still occur if the latent heat flux is negative through sublimation, even in instances where surface  
347 temperature and/or air temperature are well below the melting point (Bonekamp et al., 2021; Brun et  
348 al., 2023; Huintjes et al., 2015). COSIPY resolves all energy fluxes ( $F$ ) at the ice surface that contribute  
349 to surface melt ( $Q_{melt}$ ):

350

$$351 F = SW_{in} \cdot (1 - \alpha) + LW_{in} + LW_{out} + Q_{sens} + Q_{lat} + Q_g + Q_{liq} \quad \text{Eq. (1)}$$

352

353 Where  $SW_{in}$  is incoming shortwave radiation,  $\alpha$  is albedo,  $LW_{in}$  and  $LW_{out}$  are incoming and outgoing  
354 longwave radiation, and  $Q_{sens}$ ,  $Q_{lat}$ , and  $Q_g$  are the sensible, latent, and ground heat fluxes (Oerlemans  
355 et al., 2001) and  $Q_{liq}$  is the heat flux from liquid precipitation; the latter variable is often neglected in  
356 ablation calculations (Cuffey and Paterson, 2010) but is of particular importance here as the Indian  
357 Summer Monsoon brings a significant amount of liquid precipitation to the lower reaches of Khumbu  
358 Glacier. The resulting  $F$  is equal to the energy available for surface melt ( $Q_{melt}$ ) when surface  
359 temperature ( $T_s$ ) is at melting point ( $0^\circ\text{C}$ ).  $T_s$  is used to calculate  $LW_{out}$ ,  $Q_{sens}$ ,  $Q_{lat}$ ,  $Q_g$  and to partition  
360 solid and liquid precipitation. When  $T_s$  exceeds the melting point it is reset to  $0^\circ\text{C}$  (273.15 K) and the  
361 residual  $F$  fluxes equal  $Q_{melt}$ . In this instance, subsurface melt is triggered when the energy fluxes, for  
362 example, penetrating  $SW_{in}$  warm the ice layer so that  $T_s$  exceeds the melting point of ice (Sauter et al.,  
363 2020).

364

365 The COSIPY model domain was taken from the 30-m DEM that was resampled to 200-m grid spacing  
366 following a reference simulation for 2013–2015 and sensitivity analyses, which revealed minimal  
367 impact on the results whilst greatly reducing computational expense (Fig. 4). The sensitivity of glacier  
368 mass balance to individual meteorological variables (MAAT, radiative fluxes, relative humidity, lapse  
369 rate, precipitation amount, precipitation phase, glacier surface roughness) was calculated in sensitivity  
370 experiments using the reference simulation that perturbed these variables individually. Perturbations  
371 were made within the range of the possible uncertainties for each variable that arise from a combination  
372 of the choice of observations or climate models, the downscaling approach used, and the distribution of  
373 meteorological variables (see Section 3.1). The values used for perturbations of MAAT and  
374 precipitation amount were similar to those expected for possible future climate forcings. We tested a  
375 range of lapse rates from  $-3.0^\circ\text{C km}^{-1}$  to  $-6.0^\circ\text{C km}^{-1}$  while maintaining the same ELA based on the  
376 range of monthly values calculated from regression of NASA MODIS land surface temperature data for  
377 the Central Himalaya, which resulted in a difference in ice volume of  $0.4 \times 10^9 \text{ m}^3$  and no change in  
378 glacier length at the present day (result not shown).

379

380 The downscaled and disaggregated CORDEX RCM daily climate variables (temperature, precipitation,  
381 the radiation components, wind speed, relative humidity and atmospheric pressure) were used to force  
382 COSIPY for the periods 2015–2020 CE and 2095–2100 CE. While snowfall measurements can be used  
383 as an input to COSIPY, there are no good-quality measurements of snowfall in the Everest region and

384 so precipitation was partitioned into rainfall and snowfall using the snow transfer scheme within  
 385 COSIPY (Sauter et al., 2020). COSIPY was forced using hourly meteorology with nine variables to  
 386 calculate the energy balance and mass balance components at an hourly time step from the sum of  
 387 accumulation by solid precipitation, deposition, and refreezing of melt water percolation, and ablation  
 388 by melt and sublimation. The exchange processes at the surface, including energy release and  
 389 consumption with phase changes, control temperature distribution and phase changes within the glacier  
 390 (comprised of horizontal ice and snow layers), and accounts for meltwater refreeze and percolation with  
 391 the meltwater produced from the surface melt calculations acting as an input. The impacts of  
 392 supraglacial debris on ablation and of snow avalanching on accumulation were handled in iSOSIA, as  
 393 described in the next section.

394

## 395 **2.6 Ice-dynamical glacier evolution modelling**

396 The second-order shallow ice approximation model (iSOSIA) is a 3-D higher-order ice-dynamical  
 397 glacier evolution model that solves for the flow of ice including longitudinal and transverse stress  
 398 gradients that are imposed on ice flow through high-relief topography (Egholm et al., 2011). This glacier  
 399 model simulates the evolution of debris-covered glaciers by incorporating the feedbacks between debris  
 400 transport, mass balance and ice flow (Rowan et al., 2015) and includes two processes that are important  
 401 for many Himalayan glaciers; (1) the redistribution of snow by avalanching that is estimated to account  
 402 for up to 75% of accumulation, and (2) the formation and evolution of a supraglacial debris layer that  
 403 insulates the ice surface to modify ablation (Rowan et al., 2015). While previous versions of this glacier  
 404 model used depth-integrated ice flow, this version simulates ice flow through Khumbu Glacier in 3-D  
 405 as the ice thickness is divided into 20 vertical layers to calculate englacial debris transport (Rowan et  
 406 al., 2015). The glacier model has a variable time step that can adjust up to a maximum of 0.1 years to  
 407 allow greater computational efficiency.

408

409 The distributed surface mass balances calculated using COSIPY using the downscaled RCMs for the  
 410 periods 2015–2020 CE and 2095–2100 CE were used as inputs to the glacier model with no change in  
 411 forcing applied between these two periods. The model domain topography was the same in iSOSIA as  
 412 that used in COSIPY. Surface processes within the glacier model modified the distribution of  
 413 accumulation and ablation but this was not updated into the surface topography used in COSIPY.  
 414 Simulated accumulation was the result of the total snowfall in each cell and avalanching of snow  
 415 imposed for the accumulated snowpack from hillslopes by removing snow and ice from hillslopes  
 416 greater than 28° and redistributing this mass across less steep surfaces using a non-linear hillslope flux  
 417 model (Roering et al., 1999). The avalanching routine was found to be sufficient to prevent snow and  
 418 ice accumulation on slopes that are observed to be free of glacier ice such as the southwest face of  
 419 Sagarmatha (Mt. Everest) while allowing accumulation on steep sections of the glacier (Rowan et al.,  
 420 2015) resulting in accumulation rates at the glacier surface in line with the limited available  
 421 observations for Himalayan glaciers of 2 m water equivalent (w.e.) per year (Benn and Lehmkuhl,  
 422 2000).

423

424 Rock avalanching is responsible for much of the debris accumulation on the glacier surface but there is  
 425 little information about the magnitude and frequency of these events, so headwall erosion was assumed  
 426 to be uniform at 1 mm a<sup>-1</sup> (Rowan et al., 2021). Debris produced by headwall erosion was delivered to  
 427 the glacier surface using a similar non-linear hillslope flux model to snow avalanching. The reduction  
 428 in ablation beneath supraglacial debris from clean-ice values was represented as a reciprocal function  
 429 that scaled clean-ice ablation ( $b_{clean}$ ) to give sub-debris melt ( $b_{debris}$ ) as a function of debris thickness  
 430 ( $h$ ):

431

$$432 \quad b_{debris} = b_{clean} \times \frac{h_0}{h + h_0} \quad \text{Eq. (2)}$$

433

434 where  $h_0$  is a constant representing the characteristic debris thickness at which the reduction in ablation  
 435 due to insulation by supraglacial debris is 50% of the value for an equivalent clean-ice surface  
 436 (Anderson and Anderson, 2016; Rowan et al., 2021). The observed heterogeneity of surface ablation  
 437 required a parameterisation of sub-debris melt representing the effects of differential ablation, which

438 was represented in Equation (2) using a value for  $h_0$  of 0.8 m (Bartlett et al., 2021; Rowan et al., 2021;  
439 Strickland et al., 2023). We note that Equation (2) represents an empirical calculation of the impact of  
440 supraglacial debris on glacier surface melt that is calibrated to observations of sub-debris melt rates for  
441 glaciers in the Central Himalaya (Rowan et al., 2021) and as such, changes in surface energy balance  
442 processes including vapour fluxes within the debris-covered section of the glacier are not included.  
443

### 444 3. Results

#### 445 3.1 COSIPY parameter perturbations

446 The spatially averaged mass balance was most sensitive to changes in MAAT (perturbed by  $\pm 1.5^\circ\text{C}$ ,  
447  $2.0^\circ\text{C}$  and  $3.0^\circ\text{C}$ ),  $LWin$  and  $SWin$  ( $\pm 10\%$  and  $20\%$ ). Perturbations of relative humidity ( $\pm 10\%$  and  
448  $\pm 20\%$ ) had the least impact on mass balance. The use of a seasonal lapse rate of  $5.38^\circ\text{C km}^{-1}$  yielded a  
449 spatially averaged mass balance that was 5.6% less than the reference calculation value, while a diurnal  
450 lapse rate gave a mass balance that was only 0.45% lower because the reference lapse rate was close to  
451 the mean of the day/night lapse rates, whereas the environmental lapse rate ( $6.50^\circ\text{C km}^{-1}$ ) gave a mass  
452 balance that was 1.24% higher than the reference value. The relatively small difference in mass balance  
453 due to the choice of lapse rate is due to the extremely high elevation of Khumbu Glacier, which means  
454 that MAAT is below  $0^\circ\text{C}$  in the accumulation area for much of the year and a higher lapse rate does not  
455 affect rain/snow partitioning. The largest difference in mass balance due to the choice of lapse rate  
456 occurred just below the ELA and resulted in a difference of  $\pm 24\%$  in spatially averaged mass balance  
457 for this section of the glacier. The National Geographic AWS on Mt. Everest provided an opportunity  
458 to examine lapse rates at the highest elevations. For the period April–November 2019, the observed  
459 lapse rate was  $4.68^\circ\text{C km}^{-1}$  between Phortse (3,810 m a.s.l.) and Everest Base Camp (5,315 m a.s.l.),  
460 and  $5.36^\circ\text{C km}^{-1}$  between Camp II and South Col, similar to the value used in this study. The lapse rate  
461 above 8,000 m a.s.l. was about  $1.2^\circ\text{C km}^{-1}$  greater than that below 5,600 m a.s.l. between the two highest  
462 AWS at the South Col (7,945 m a.s.l.) and the Balcony (8,430 m a.s.l.) indicating that in the highest-  
463 elevation sections of the catchment, lapse rates may be best represented by values considered suitable  
464 for the free atmosphere.  
465

466 Coupled parameter testing was carried out to perturb precipitation and MAAT simultaneously. The most  
467 significant change in spatially averaged mass balance followed a  $3^\circ\text{C}$  increase in MAAT and 20%  
468 decrease in precipitation amount. The change in ablation following an increase in temperature of  $1.5^\circ\text{C}$   
469 was compensated by accumulation resulting from 20% higher precipitation. The impact on mass  
470 balance of two precipitation phase (rain/snow) partitioning schemes was investigated and compared  
471 with the default snow transfer function in COSIPY; (1) using threshold temperatures of  $0.5^\circ\text{C}$ ,  $2.0^\circ\text{C}$ ,  
472 and  $3.5^\circ\text{C}$ , and (2) using a calculation that smoothly scaled rain/snow partitioning from 100% solid  
473 precipitation at  $-1^\circ\text{C}$  to 0% solid precipitation at  $4^\circ\text{C}$ . The height of the  $0^\circ\text{C}$  isotherm during months  
474 that experienced significant ablation (May–September) fluctuated around 5,125–6,250 m a.s.l., which  
475 correlated with the elevations that experienced the greatest mass balance change with lapse rate. While  
476 the lapse rate used to distribute MAAT did not have a significant impact on glacier-wide mass balance,  
477 the elevation of the  $0^\circ\text{C}$  isotherm from the pre-monsoon until the end of the monsoon was sensitive to  
478 the air temperature distribution.  
479

480 The glacier ice surface roughness ( $z_0$ ) value was 1.7 mm (Table 2), which is a reasonable estimate for  
481 clean-ice glaciers (Mölg et al., 2012). The  $z_0$  values reported in the literature vary widely, even for clean-  
482 ice glaciers, and do not consider debris-covered glacier surfaces, and so two substantially different  $z_0$   
483 values were tested as end-members of the likely range in  $z_0$  values for Khumbu Glacier. Values for  $z_0$  of  
484 0.1 mm from Midtre Lovénbreen in Svalbard (Irvine-Fynn et al., 2014) and August-One Glacier in  
485 China (Guo et al., 2018), and a value of 6.9 mm for the clean-ice section of Haut Glacier D’Arolla  
486 (Brock et al., 2006) were all tested in the reference simulation. Adjusting  $z_0$  had minimal impact on  
487 mass balance, although a higher (lower)  $z_0$  did result in slightly increased (decreased) mass balance.  
488

#### 489 3.2 Evaluation of the COSIPY surface energy balance model results

491 The reference simulation represented the period 2013–2015 CE and was forced with AWS data using  
492 the model parameters in Table 2. Turbulent fluxes and energy balance components across Khumbu

493 Glacier were explored across the 2013–2015 reference period to assess the performance of COSIPY  
494 and understand their relative spatial importance (Fig. 5). The glacier-wide clean-ice mass balance for  
495 the three-year reference period was  $-3.4$  m w.e, which equates to  $-1.13$  m w.e  $a^{-1}$ . Maximum ablation  
496 was up to 16.2 m w.e. over three years (Fig. 4). High precipitation events were observed to offset some  
497 ablation if they occurred outside the core monsoon season (e.g., in October 2013 and May 2014) but  
498 did not influence monsoon season ablation when high air temperatures and strong incoming radiative  
499 fluxes rapidly remove snow cover and drive melting. Higher minimum temperatures in winter 2013–  
500 2014 CE relative to the other winters did not significantly influence accumulation rates, which remained  
501 similar to those in 2014–2015 CE. Low precipitation amounts during the 2015 monsoon (286 mm in  
502 2015, compared to 330.8 mm in 2013, and 333.9 mm in 2014) resulted in lower accumulation in the  
503 upper reaches of the glacier. The precipitation gradient was calibrated to  $1 \times 10^{-5} \% m^{-1}$  to match  
504 observed accumulation rates. However, this gradient largely arises from avalanching (Benn and  
505 Lehmkuhl, 2000) which is challenging to represent in COSIPY and was instead handled in the glacier  
506 model (Section 2.6).

507  
508 The energy available for ablation peaked in the pre-monsoon and monsoon, bringing higher rates of  
509 sublimation and subsurface melt in April–June (Fig. 5). Simulated sublimation occurred at all  
510 elevations, with the highest cumulative loss near the South Col (EB7910) where sublimation dominated  
511 mass balance and only slightly slowed from December until May. Sublimation rates were increasingly  
512 tied to seasonality with distance down-glacier, with rates on the lower section of the tongue (EB4980)  
513 increasing from April until the start of the monsoon in July. Calculated subsurface melt was negligible  
514 at or above the ELA (5,950 m a.s.l.) whereas at lower elevations sub-surface melt dominated mass  
515 balance with a stronger seasonal cycle related to surface temperature. The interannual variability in  
516 subsurface melt was linked to surface temperature, although low simulated subsurface melt rates in the  
517 first year of the reference simulation were largely due to persistence of the initial snow cover that  
518 shielded the subsurface from relatively warm air temperatures until the subsurface adapted to local  
519 conditions. Refreezing occurred across the entire glacier, with a staggered onset due to increased  
520 elevation, and the absolute values were low (Fig. 5). The higher latent heat flux during the monsoon  
521 resulted in higher deposition of snow to the glacier at the lower elevations, with negligible rates at  
522 higher elevation. Similar absolute values and patterns are seen for condensation.

523  
524 Calculated incoming shortwave radiation matched well with AWS observations, indicating that the  
525 radiation model in COSIPY performed well across the extreme relief of the Khumbu Glacier catchment.  
526 Net shortwave radiation contributed the largest energy input to the glacier surface at lower elevations,  
527 correlating most strongly with the energy available for melt, with a mean correlation coefficient of 0.79.  
528 There was high temporal variability related to variable cloud cover exhibited in the hourly incoming  
529 shortwave radiation forcing and fluctuating albedo during the warmer months with the melting of the  
530 snowpack. The high incoming shortwave radiation the upper reaches of the glacier indicate that low net  
531 shortwave radiation is not due to topographic shading. Net shortwave radiation was correlated with  
532 albedo ( $r = 0.86$ ), and the persistence of snow throughout much of the year reduced the energy available  
533 for melt. Net longwave radiation also contributed to the energy available for melt as the pattern of both  
534 fluxes corresponded. Between 5,900–7,900 m a.s.l., net longwave radiation sometimes exceeded zero  
535 during the monsoon, most likely due to heavy cloud cover and increased temperatures relative to the  
536 glacier surface. The latent heat flux was almost zero at the lower elevation sites as the arrival of the  
537 monsoon resulted in higher relative humidity, and this pattern was similar, but dampened, at higher  
538 elevation. At the South Col (EB7910) the energy available for melt correlated most closely with the  
539 sensible heat flux (Fig. 5).

540  
541 Grid spacings for the model domain of 30 m, 50 m, 200 m and 1 km were tested to ensure that that the  
542 COSIPY calculations captured orographic effects without unnecessary computational expense (Fig. 4).  
543 The simulated maximum accumulation rate did not change significantly with grid spacing, giving  
544 accumulation rates of 2.1–3.9 m w.e. at 6,500–7,000 m a.s.l. in the reference simulation. The 1 km grid  
545 spacing contained only 27 glacier points, and gave a similar spatial mean mass balance to the finer-  
546 resolution calculations, but there were large gaps in mass balance calculated across the glacier that  
547 affected the height of the ELA and significantly reduced the calculated maximum accumulation value.

548 The 30-m and 50-m grid spacings captured greater spatial variability in mass balance relative to the 200  
549 m resolution calculation, particularly at elevations between 5200–5400 m a.s.l. (Fig. 4). However, as  
550 the ELA, and the calculated maximum and minimum mass balances were not significantly different  
551 between these finer-resolution calculations, the 200 m grid spacing was used throughout to benefit from  
552 the much reduced computational expense.

553

### 554 **3.3 Evaluation of the RCM downscaling**

555 The downscaled climate variables from the three RCMs for the present-day time slices (2015–2020 CE)  
556 were evaluated against 14 years of observations from three AWS to assess the representation of means,  
557 seasonality, diurnal cycles, day-to-day variability, and interannual variability (Fig. 2C and 2D). All three  
558 downscaled RCMs showed good agreement between MAAT ( $-2.15 \pm 0.05^\circ\text{C}$ ) and observed air  
559 temperature from the Pyramid AWS (Figs. A1 and A2). The representation of the monsoon was greatly  
560 improved by the RCM downscaling; temperature seasonality was well resolved following quantile  
561 mapping and the monthly mean and minimum air temperatures were similar to observations across the  
562 present-day time slice (Fig. A1). The monsoon stabilised air temperatures and reduced the range  
563 between minimum and maximum temperatures in the downscaled RCMs, which was in better  
564 agreement with AWS observations, but was not present in the raw RCMs prior to downscaling. We note  
565 that the downscaled maximum air temperature was at times higher than observations amongst all RCMs  
566 during the post-monsoon and winter (Fig. A1) but the distribution of downscaled air temperatures was  
567 similar to observed values (Fig. A2). Gamma-distribution quantile mapping substantially improved the  
568 absolute precipitation values relative to the AWS observations compared to those in the raw RCMs; the  
569 overestimation of winter precipitation and relative underestimation of monsoon precipitation amounts  
570 in the raw RCMs was reduced and downscaled results show a clearer monsoon signal (Fig. A3). When  
571 compared with AWS observations, RCM downscaling slightly overcorrected the seasonal precipitation  
572 pattern with a slight underestimation of winter precipitation for the most extreme winter events. Across  
573 the three present-day RCM simulations, the surface mass balance calculated using the NOAA RCM  
574 was more positive than that for the ISPL and CCCma RCMs and most similar to the mass balance  
575 calculated from meteorological observations, and remained the most positive mass balance in the end-  
576 of-century time slices (Fig. 6).

577

### 578 **3.4 Evaluation of the iSOSIA glacier evolution model results**

579 COSIPY was used to calculate clean-ice surface mass balance from the downscaled RCMs, and the  
580 insulating effects of supraglacial debris were calculated in iSOSIA. The simulated glacier geometry and  
581 dynamics were compared with remotely sensed observations of ice thickness, supraglacial debris  
582 distribution, velocity, and surface elevation change for the present-day glacier (Fig. 3) and varied  
583 depending on the RCM used as forcing (Fig. 7). The experiment using the NOAA RCM was identified  
584 as the starting point for all future simulations because this was most representative of the observed  
585 glacier at 2015 CE (Fig. 3). The distributed surface mass balances calculated using COSIPY were most  
586 similar to observed values after the calculated surface mass balances were integrated with the glacier  
587 model to include accumulation by snow avalanching and the reduction in surface melting beneath  
588 supraglacial debris; the active glacier extent was underestimated if supraglacial debris is not simulated  
589 (Fig. 8). The supraglacial debris-mass balance feedback in the glacier model reproduced the observed  
590 reversed mass balance gradient and peak in ablation below the Khumbu Icefall (Fig. 1D).

591

592 The simulated glacier area was  $7.8 \text{ km}^2$  and similar to that obtained from structural mapping in 1979  
593 CE (Nakawo, 1986). Radio-echo sounding in 1999 CE obtained ice thickness estimates close to the  
594 active terminus of  $\sim 160 \text{ m}$  (Gades et al., 2000) and simulated ice thickness at the terminus was  $130 \text{ m}$   
595 (Fig. 3A). The simulated thickness at the active glacier terminus thickness was approximately  $175 \text{ m}$  in  
596 1999 CE, which agreed well with observations from DEMs of difference that show thinning here of up  
597 to  $55 \text{ m}$  between 1984–2018 CE (Fig. 3D and 3E) (King et al., 2020). Simulated surface elevation  
598 change in the ablation area was  $-30 \text{ m}$  over 20 years to the present day and similar to values derived  
599 from satellite observations for 1984–2018 CE (King et al., 2020). Simulated present-day glacier  
600 velocities (Fig. 9) reached a maximum of  $248 \text{ m a}^{-1}$  and showed a similar pattern and magnitude to  
601 glacier surface velocities observed using remote sensing observations, which reach a maximum of  $220$   
602  $\text{m a}^{-1}$  in the Khumbu Icefall (Altena and Käab, 2020) and up to  $20 \text{ m a}^{-1}$  in the ablation area (Quincey

603 et al., 2009; Dehecq et al. 2019). The simulated present-day velocities in this study were a better fit to  
604 remote sensing observations than those from previous simulations that used an elevation-dependent  
605 mass balance forcing (Rowan et al., 2015, 2021) where the maximum simulated velocities were 118 m  
606  $\text{a}^{-1}$ .

607

### 608 **3.5 Climate change and glacier evolution from the present day until 2100 CE**

609 Khumbu Glacier is responding to historical climate change and will continue to shrink even if warming  
610 ceases today. Indeed, if we allow the spin-up experiment to reach equilibrium with the present-day  
611 NOAA RCM mass balance, the glacier terminus will recede by 2.1 km and the maximum ice thickness  
612 will decrease from 246 m to 206 m by 2100 CE without any additional warming. In this scenario, a  
613 supraglacial debris layer up to 1.3 m thick extends 1 km up-glacier from the terminus and partially  
614 dampens the committed volume loss, by sustaining 13% more ice volume than would be the possible  
615 for a clean-ice glacier surface with the same mass balance (Fig. 10A). The committed glacier volume  
616 loss due to historical warming in the absence of any further climate forcing is 10–23% of the present-  
617 day glacier mass (Fig. 10C) with the associated uncertainty represented by this range of values arising  
618 from the parameterisation of the impact of supraglacial debris evolution on surface melting.

619

620 Now considering the effects of additional warming under the RCP scenarios for the NOAA experiment,  
621 we find that greater warming occurs in winter than in the monsoon under both RCPs and results in an  
622 increase in annual precipitation amount of about 15% made up of a greater increase in non-monsoon  
623 precipitation than monsoon precipitation (Fig. 2E). The climate forcing from the downscaled NOAA  
624 RCM under RCP4.5 is 1.4°C warmer than the present day ( $-0.75^\circ\text{C}$  in 2095–2100 CE compared with  
625  $-2.15^\circ\text{C}$  in 2015–2020 CE) and annual precipitation increases by 14.8% from 581.4 mm at present day  
626 to 664.8 mm  $\text{a}^{-1}$  by 2100 CE with monsoon (June–September) precipitation increasing by 5.4% and  
627 non-monsoon season (December–February) precipitation increasing by 14.1% (Fig. 2E). Under  
628 RCP8.5, the downscaled climate forcing is projected to be 3.8°C warmer than present day ( $1.65^\circ\text{C}$  in  
629 2095–2100 CE) with an increase in annual precipitation of 14.9% by 2100 CE, with monsoon  
630 precipitation increasing by 9.8% and non-monsoon precipitation increasing by 19.4% (Fig. 2E).

631

632 In the NOAA RCM RCP4.5 experiment, the spatially averaged cumulative glacier mass balance is  $-$   
633  $0.14 \text{ m w.e. a}^{-1}$  in 2100 CE, which is slightly more positive than the present-day value of  $-0.21 \text{ m w.e.}$   
634  $\text{a}^{-1}$  (Fig. 6) and glacier volume decreases by 36% between the present day and 2100 CE (Fig. 10C).  
635 While significant, this end-of-century glacier loss is partially offset by the concurrent increase in  
636 precipitation. In comparison, an equivalent simulation forced only by warming and without any change  
637 in precipitation results in a more linear trajectory of glacier change and 70% loss of glacier volume by  
638 2100 CE (cyan line in Fig. 10C) demonstrating that 34% of potential glacier loss from warming could  
639 be compensated by the increase in precipitation that occurs as a result of warming.

640

### 641 **3.6 Comparison of projections for different RCM forcings**

642 The CCCma and IPSL RCMs projected greater warming from the present day by 2100 CE than the  
643 NOAA RCM under RCP4.5 with a value of  $1.6^\circ\text{C}$  ( $+0.2^\circ\text{C}$  compared with the NOAA RCM) in the IPSL  
644 RCM experiment and  $2.2^\circ\text{C}$  ( $+0.8^\circ\text{C}$ ) in the CCCma RCM experiment. These two RCMs also projected  
645 slightly greater warming by 2100 CE under RCP8.5, with a value of  $3.9^\circ\text{C}$  ( $+0.1^\circ\text{C}$  compared with the  
646 NOAA RCM) for the IPSL RCM experiment and  $4.1^\circ\text{C}$  ( $+0.3^\circ\text{C}$ ) for the CCCma RCM experiment.

647

648 The projected increase in precipitation amount across the three RCMs is similar between RCPs with  
649 annual totals above 600 mm by 2100 CE. The CCCma RCM gives the greatest increase in annual  
650 precipitation amount of 100 mm by 2100 CE (Fig. 2E). There is no evidence of change in the intensity  
651 of the Indian Summer Monsoon, as the seasonal split in precipitation remains similar to the present day,  
652 but the frequency of days with high precipitation (over 15 mm per day) increases by 2100 CE, giving  
653 twice as many days in the NOAA RCM experiment and up to seven times as many days in the IPSL  
654 RCM experiment.

655

656 Under RCP8.5, all experiments showed similar results for mass balance by 2100 CE with only a 10%  
657 difference in glacier volume between the three RCMs (Fig. 10C). The CCCma RCM experiment has

658 only a 1% difference in volume loss between RCP4.5 and RCP8.5 by 2100 CE despite a 1.9°C  
659 difference in MAAT—this is a surprising result given the significant temperature difference, which can  
660 be attributed to the greater number of high-magnitude precipitation events that occur under RCP8.5 in  
661 combination with the small difference in winter temperatures between the two RCPs. Indeed, in the  
662 CCCma RCM experiment under RCP4.5, the maximum winter temperature is 1.7°C higher than for the  
663 other RCMs, resulting in ablation and rainfall (rather than snowfall) during the winter.  
664

#### 665 4. Discussion

##### 666 4.1 Uncertainties associated with the glacier modelling

667 Sources of uncertainty in our results arose from each step of our glacier modelling workflow, and we  
668 considered how the experiments could be designed to reduce these uncertainties. Here we discuss the  
669 potential sources of uncertainty associated with the choice of RCMs, the downscaling of the RCMs, the  
670 use of time slices rather than continuous mass balance calculations, the representation of future  
671 precipitation in the RCMs, and the representation of avalanching in the glacier model.  
672

673 A single RCM was not considered sufficient to represent both present-day climate and potential future  
674 climatic extremes, but the climate-mass balance forcing ensemble was limited in size due to the small  
675 number of RCMs available. The use of three RCMs allowed the implications of uncertainties in  
676 understanding of local climate for glacier evolution to be evaluated. A multi-model mean approach  
677 using all the CORDEX South Asia RCMs (as widely used elsewhere) was not considered sufficient to  
678 represent present-day and future climate conditions in the Khumbu Valley because this approach gives  
679 equal weighting to models irrespective of their performance (Pierce et al., 2009) and does not enable  
680 intercomparison of results for future climate conditions.  
681

682 Five-year downscaled RCM time slices were chosen to reduce computational expense associated with  
683 COSIPY and the integration with iSOSIA. To ensure that the five-year periods selected were  
684 representative, the preceding decade was used for comparison with the time-slice results (results not  
685 shown). The use of quantile mapping with 14 years of AWS data as the downscaling method limited the  
686 influence of any natural variability by ensuring that the period did not reflect an extreme phase of natural  
687 climate oscillation. This comparison was particularly important for the future time slices, where large  
688 uncertainties arise between RCMs, and observational data cannot be used for evaluation of the  
689 downscaled climate or the resulting mass balance. We note that this experimental design could be  
690 improved by interpolating the mass balance over time and coupling the COSIPY and iSOSIA models  
691 such that mass balance was calculated dynamically for the evolving ice surface, but this was beyond  
692 the scope of our experiments. However, the experiments were repeated using additional mid-Century  
693 (2045–2050 CE) mass balance forcings to investigate if this produced a different end-of-Century result.  
694 These experiments produced near-identical results in 2100 CE to the experiments with no mid-Century  
695 forcing, in part because the response time of the simulated glaciers was longer than the 40-year period  
696 between the present-day and future time slices. Thus, a mid-century surface mass balance forcing was  
697 not considered necessary in our experiments and instead we used a step forcing for mass balance rather  
698 than interpolation between mass balance calculations in the glacier model.  
699

700 The differences in simulated glacier change and response time between RCM forcings were at times  
701 greater than those resulting from the RCP due to differences in projections of precipitation. Whilst the  
702 three selected RCMs performed well in representing annual precipitation cycles from the six available  
703 CORDEX RCMs, we note that this representation was still fairly poor, although substantially improved  
704 by quantile mapping (Fig. 2D). The poor representation of monsoon dynamics in the present-day RCMs  
705 highlights an additional uncertainty associated with future precipitation scenarios and that these results  
706 should be treated as a set of possible scenarios.  
707

708 The CORDEX CMIP5 and CMIP6 projects only produced dynamically downscaled RCMs for two  
709 future emissions scenarios (RCP4.5 and RCP8.5) and as such the implications of other RCPs for glacier  
710 evolution could not be assessed. The downscaled future climates were compared with those from other  
711 studies using CORDEX results, and showed similar annual and seasonal regional temperature trends  
712 strongly linked to the choice of RCP, and similar positive precipitation trends with poor agreement

713 between RCMs (Kaini et al., 2019; Sanjay et al., 2017). The relationship between precipitation and  
714 warming in the two future emissions scenarios was less clear than that for air temperatures because the  
715 monsoon-influenced Himalaya has particularly poor RCM consensus and high levels of uncertainty in  
716 future precipitation trends with warming relative to other regions in High Mountain Asia (Sanjay et al.,  
717 2017).

718  
719 A potentially large uncertainty in the glacier model arose from the parameterisation of avalanching, as  
720 this mass balance variable is poorly constrained, with no direct observations of the avalanche  
721 contribution to the mass balance of Khumbu Glacier and high regional variability (Kneib et al., 2025).  
722 Avalanching was included in iSOSIA by slope-dependent diffusion and resulted in increased  
723 accumulation along the glacier surface in the Western Cwm and improved the agreement between  
724 simulated and estimated accumulation rates and distribution (Fig. 1D). Future work to resolve the  
725 impact of low frequency–high magnitude avalanche events on accumulation rates would be useful to  
726 refine this calculation but the contribution of avalanches to glacier accumulation over decadal time  
727 scales remains extremely challenging to measure (Purdie et al., 2025).

#### 728 729 **4.2 Impacts of mesoscale and microscale meteorology on glacier change**

730 Our study addresses fine-scale temporal (hourly) and spatial (100 m) glacier surface processes,  
731 including avalanching and sublimation, that affect glacier surface mass balance across the elevation  
732 range of Khumbu Glacier, but further observations of meteorological and glaciological conditions at  
733 the highest elevations would be beneficial, and are needed if micro-scale processes are to be included  
734 in glacier models (Brun et al., 2023; Khadka et al., 2021; Mölg et al., 2014; Shaw et al., 2022). Analysis  
735 of meteorological observations from AWS across the Dudh Koshi catchment indicated that precipitation  
736 gradients were weak, slightly negative or absent, confirming the observations of Salerno et al. (2015)  
737 and Yang et al. (2017). To test the sensitivity of precipitation to elevation, COSIPY was forced by a  
738 gridded climate distributed using weak negative, weak positive, and no precipitation gradients  
739 distributed across the model domain using a linear regression with elevation from the 100-m resolution  
740 DEM. The results of these experiments were used to force iSOSIA and the simulated historical glacier  
741 evolution was similar, resulting in only a 10 m difference in the maximum ice thickness between  
742 simulations with different precipitation gradients (result not shown).

743  
744 The mass balance sensitivity to seasonal and daily variations in lapse rate showed a lesser impact on  
745 glacier-wide mass balance than in other studies, due to the large elevation range of Khumbu Glacier  
746 whereby a smaller fraction of the glacier relative to total area is located along the zero degree isotherm  
747 (e.g., compared to Yala Glacier in Nepal; Immerzeel et al., 2014). Seasonal and daily lapse rates that  
748 accounted for marked lower values during the monsoon season and at night gave a mean annual value  
749 of  $5.54\text{ }^{\circ}\text{C km}^{-1}$ , which produced glacier-wide mass balance and ice thickness simulations that were  
750 closest to geodetic observations and represented the maximum rates of surface lowering in the upper  
751 ablation area where the debris layer is thinnest (Fig. 3D and 3E).

752  
753 Sublimation simulated in our study occurred at all elevations with the highest rate of ice loss due to  
754 sublimation ( $-0.12\text{ m w.e. a}^{-1}$ ) in the upper reaches of the Khumbu Glacier catchment near to South Col  
755 (about 7,495 m a.s.l.) where sublimation dominated ablation with only minor seasonality (Fig. A6).  
756 Whilst this amount of ice loss by sublimation is not negligible, it is almost half that found in the point-  
757 based calculations after adjusting for the different time periods represented by our studies (Matthews et  
758 al., 2020), which is likely due to the assumed uniformity of wind speed across the model domain in  
759 COSIPY. Future work to improve the calculation of sublimation in distributed surface mass balance  
760 calculations for high-elevation glaciers would be valuable.

761  
762 While we have considered the effects of mesoscale meteorology on glacier mass balance, smaller-scale  
763 processes operating close to the land surface could also be important. Katabatic winds were suggested  
764 to explain a local 15-year decrease in maximum air temperatures and precipitation over glaciers while  
765 minimum air temperatures continued to rise (Salerno et al., 2023). However, this effect was found to be  
766 short-lived (Shaw et al., 2025) and the impact of microscale near-surface cooling on the duration and  
767 extent of mesoscale precipitation and accumulation is likely to be minimal and therefore unlikely to

768 significantly affect glacier-wide mass balance (Mott et al., 2020; Shaw et al., 2024). Observations from  
769 the Camp 2 AWS (6,464 m a.s.l.) indicate that surface energy fluxes may be sufficient to cause non-  
770 negligible melting of glacier surfaces despite freezing air temperatures (Matthews et al., 2020). Results  
771 from an ice core from South Col Glacier (>8,000 m a.s.l.) combined with COSIPY experiments  
772 suggested that ablation may also take place at even at the highest elevations (Potocki et al., 2022).  
773 However, a subsequent study found no evidence of glacier mass change, and identified large  
774 uncertainties associated with simulating mass balance at these extreme elevations where sub-daily air  
775 temperature gradients and the duration of snow cover strongly affect ablation and accumulation (Brun  
776 et al., 2023). Future work is needed to reduce these uncertainties, as very few observations exist of  
777 accumulation processes and the upper limit of ablation processes for high-elevation Himalayan glaciers.  
778

### 779 **4.3 Possible outcomes under RCP8.5**

780 Current global greenhouse gas emissions are following the trajectory of the intermediate emissions  
781 scenario RCP4.5, while the high emissions scenario RCP8.5 could be described as ‘low possibility but  
782 high impact’ (Pedersen et al., 2020). However, as represented in the RCMs used in our study, mountain  
783 regions are warming more rapidly than the global mean such that a global temperature rise of 1.5°C will  
784 lead to  $2.1 \pm 0.1^\circ\text{C}$  of warming in High Mountain Asia (Kraaijenbrink et al., 2017; Pepin et al., 2022)  
785 although the occurrence of elevation-dependent warming above 5,000 m a.s.l. is debated (Gao et al.,  
786 2018). The high temperatures projected under RCP8.5 could potentially be offset partly by increased  
787 precipitation, given that high-magnitude precipitation events from winter Westerly disturbances  
788 increased by a factor of seven between present day and 2100 CE in the IPSL RCM under RCP8.5.  
789

790 We found no evidence of future increases in precipitation offsetting RCP8.5 warming; net glacier mass  
791 balance was strongly negative in all RCP8.5 experiments and insufficient to maintain any actively  
792 flowing glacier. Under RCP8.5, glacier mass balance in the monsoon-influenced Himalaya may  
793 therefore shift from being driven by accumulation during the monsoon to predominantly during winter.  
794 Monsoon precipitation would only result in snow accumulation at the very highest elevations and would  
795 be insufficient to maintain flowing glaciers. This outcome is avoidable by limiting anthropogenic  
796 warming to within RCP4.5, which, due to the associated increase in precipitation, could sustain nearly  
797 two thirds of the current glacier volume until 2100 CE and potentially for two centuries further into the  
798 future.  
799

### 800 **4.4 Comparison with global glacier modelling results**

801 A recent global glacier modelling study forced by an ensemble of 10 GCMs projected mass loss of 64%  
802 for Khumbu Glacier by 2100 CE (Rounce et al., 2023). In comparison, our experiments project less  
803 severe rates of decline, resulting in 30% less mass loss under the RCP4.5 future climate scenario than  
804 in the global study (Fig. 10C). One difference between these results is that rather than using the global  
805 glacier inventory outline to define the glacier margins we consider only the actively flowing glacier and  
806 so exclude 20% of the starting glacier volume in the detached tongue. We would expect the two sections  
807 of the glacier to evolve along different paths; while the active glacier responds to climate change as  
808 projected in our experiments, thick supraglacial debris mantling the detached tongue could allow this  
809 ice mass to survive and slowly decay *in situ* for many decades beyond the present day. The decay of the  
810 detached tongue may however increase due to erosion of the surface by ice cliffs and supraglacial water  
811 bodies that are expanding across the former glacier surface (King et al., 2020).  
812

813 Our experiments only consider the rapidly changing active glacier, and we expect that the debris-  
814 covered tongue would melt more slowly than projected in the global modelling study, but as we do not  
815 consider the stagnant tongue to be part of the present-day glacier the ice volume simulated at the start  
816 of our experiments is smaller than that represented by Rounce et al. (2023) and other studies based on  
817 the RGI glacier inventory. The dynamically detached debris-covered tongue represents about 20% of  
818 the present-day glacier volume and contains ice estimated as up to 360 m thick. The mean present-day  
819 ablation rate across this section of the glacier simulated in Rowan et al. (2021) is  $-0.54 \text{ m w.e. a}^{-1}$  which  
820 can be used to estimate the life expectancy of the debris-covered tongue assuming no input of ice from  
821 the active glacier and no change in ablation rate due to thickening of supraglacial debris or the  
822 development of ice cliffs and supraglacial ponds. While the thickest part of the detached tongue may

823 survive for ~600 years, the mean life expectancy of this ice mass is  $176 \pm 148$  years from the present  
824 day meaning that the former debris-covered tongue will vanish by 2200 CE.

825

#### 826 **4.5 The response of large debris-covered glaciers to climate change**

827 The dynamic response time of large glaciers to climate change is of the order of centuries. For this  
828 reason, we start our simulations from the late Holocene (~1 ka) moraine extent when Khumbu Glacier  
829 was last considered dynamically stable (Hornsey et al., 2022; Rowan et al., 2015). The relationship  
830 between glacier response time and mass balance becomes less important after 2100 CE when the glacier  
831 is so small that ice flow has little impact on glacier volume change. Global and regional glacier  
832 modelling studies typically start their simulations in the current Century (e.g., 2000–2007 CE in  
833 Marzeion et al. (2020); 2000 CE in Rounce et al. (2023)) and a further complication arises from the use  
834 of global glacier inventories as a starting point for glacier modelling studies as such inventories cannot  
835 capture the current dynamic state of glaciers that are imbalanced, and include all ice-covered areas  
836 rather than identifying only actively flowing ice. However, satellite-derived velocity products could be  
837 used identify where ice flow within glacier outlines declines to negligible rates (Dehecq et al., 2019).

838

839 The RGI 7.0 inventory for Khumbu Glacier is based on imagery from 1999 CE (RGI 7.0 Consortium,  
840 2023) where the detached debris-covered tongue represents 20% of the glacier volume contained within  
841 this outline (Fig. 1C). Simulations that integrated the stagnant tongue into the model domain rather than  
842 as part of the flowing ice improved the representation of simulated ice flow compared to observed  
843 values, supporting our conclusion that the debris-covered tongue has been dynamically detached from  
844 the active glacier for 50–100 years (Rowan et al., 2021). Field observations support the concept of  
845 active and stagnant sections co-existing in contact with each other as englacial optical televiewing  
846 indicated that thrusting occurs at several sites, denoted by skewed internal debris layers and of basal ice  
847 that has been thrust to the glacier surface, near to the active glacier terminus from the direction of  
848 Khumbu Icefall (Miles et al., 2021). Our simulations show that development of supraglacial debris at  
849 the active glacier terminus reduced net volume loss by 13% (Fig. 8). Dynamic detachment of debris-  
850 covered tongues could allow these glaciers to move closer to equilibrium with a rapidly changing  
851 climate, the local mass balance gradient is a more important control on glacier change for both clean-  
852 ice glaciers and debris-covered Himalayan glaciers.

853

#### 854 **5. Conclusions**

855 In the monsoon-influenced Himalaya, 85% of the glacier area is located higher than 5,000 m above sea  
856 level, and 21% of this ice is above 6000 m in elevation. Despite these high elevations, Himalayan  
857 glaciers are rapidly losing ice in response to recent warming and are projected to shrink by 53% to 70%  
858 during this Century. However, the impact of future changes in precipitation on glacier loss remains  
859 uncertain, because changes in precipitation amount and distribution is often overlooked in glacier model  
860 projections. We explored the effects of future warming in tandem with changes in precipitation by  
861 simulating the evolution of Khumbu Glacier in the Everest region of Nepal using a surface energy and  
862 mass balance model forced by downscaled Regional Climate Model outputs to drive an ice-dynamical  
863 glacier evolution model. Historical warming commits Khumbu Glacier to loss of 10–23% of the total  
864 ice volume by 2100 CE. While warming due to intermediate future greenhouse gas emissions (RCP4.5)  
865 will lead to glacier volume loss of 70% by 2100 CE, the projected concurrent increase in precipitation  
866 amount will offset 34% of this and so reduce glacier loss by about a half. However, high future  
867 emissions (RCP8.5) will not be compensated by changes in precipitation amount but will instead result  
868 in substantial ablation above 6,000 m with devastating consequences for one of the highest glaciers on  
869 Earth. Our results indicate that the net mass balance of Khumbu Glacier could be close to zero in 2100  
870 CE under RCP4.5 and therefore, if climate change is limited to this intermediate emissions scenario,  
871 Khumbu Glacier will recede to the base of the icefall with insignificant further change in glacier volume  
872 beyond this point. In this scenario, Khumbu Glacier has a similar extent in 2100 CE to the active section  
873 of the present-day glacier, and represents at least one example of how monsoon-influenced Himalayan  
874 glaciers could persist into the future if global efforts are sufficient to mitigate anthropogenic climate  
875 change.

876

877

878 **Code availability**

879 The COSIPY version 1.3 glacier surface energy and mass balance model is available from the original  
880 publication describing this model (Sauter et al., 2020) and Zenodo (Arndt et al., 2020). The iSOSIA  
881 version spm-3.3.3r glacier model is available from Zenodo (Rowan and Pedersen, 2024).

882

883 **Data availability**

884 Daily data from the Coordinated Regional Downscaling Experiment (CORDEX) South Asia domain  
885 were downloaded from the Indian Institute of Tropical Meteorology website  
886 ([http://cccr.tropmet.res.in/home/cordexsa\\_about.jsp](http://cccr.tropmet.res.in/home/cordexsa_about.jsp)) for the grid box nearest to Khumbu Glacier  
887 (27.9065°N, 86.4353°E). Incoming shortwave and longwave radiation components were downloaded  
888 from the ESGF portal (<https://esgf-ui.ceda.ac.uk/cog/projects/cordex-ceda/>). Meteorological  
889 observations were derived from the Ev-K2-CNR SHARE network (<https://www.ev-k2-cnr.org>) and the  
890 GlacioClim (<https://glacioclim.osug.fr/>).

891

892 **Author contributions**

893 Conceptualisation: DJQ, ANR, AVR

894 Data curation: ASD, ANR, AVR

895 Formal analysis: ASD, ANR, AVR

896 Funding acquisition: DJQ, ANR, AVR

897 Investigation: ASD

898 Methodology: ASD, ANR, AVR, VKP

899 Project administration: DJQ, ANR

900 Resources: DJQ, ANR

901 Software: AVR, VKP

902 Supervision: DJQ, ANR, AVR

903 Validation: ASD, AVR

904 Visualisation: ASD, AVR

905 Writing – original draft preparation: ASD, AVR, DJQ, ANR, VKP

906 Writing – review and editing: ASD, AVR, DJQ, ANR, VKP

907

908 **Competing interests**

909 The authors declare that they have no conflicts of interest related to this work.

910

911 **Acknowledgements**

912 Tobias Sauter and Anselm Arndt are thanked for support in using COSIPY. We thank Patrick Wagnon  
913 for sharing the Pyramid and Changri Nup Glacier automatic weather station data. We thank David  
914 Rounce for sharing the global glacier model results for Khumbu Glacier from Rounce et al. (2023). We  
915 thank Editor Emily Collier, Emily Potter and an anonymous reviewer for their detailed and constructive  
916 comments that greatly improved the focus and clarity of this work.

917

918 **Financial support**

919 ASD was supported by the Priestley International Centre for Climate at the University of Leeds, and a  
920 University of Leeds Anniversary Research Scholarship. AVR was supported by a Royal Society  
921 Dorothy Hodgkin Research Fellowship (DHF\R1\201113). Some of the simulations presented were  
922 performed using resources provided by Sigma2, the National Infrastructure for High-Performance  
923 Computing and Data Storage in Norway.

924

925

926

927 **Tables and captions**

928

929 Table 1. Regional Climate Models (RCMs) chosen for this study and details of the Global Circulation  
 930 Models (GCMs) from which these are derived.

931

932

CORDEX South Asia regional climate model	Driving CMIP5 global climate model	CMIP5 modelling centre	RCM name in this study	Future precipitation scenario (qualitative)	2100 CE mean temperature change from present day (°C)	
					RCP 4.5	RCP 8.5
ITM-RegCM4	NOAA-GFDL-GFDL-ESM2M	National Oceanic and Atmospheric Administration (NOAA), USA	NOAA	Wet	1.4	3.8
IITM-RegCM4	CCCma-CanESM2	Canadian Centre for Climate Modelling and Analysis (CCCma), Canada	CCCma	Moderate	2.2	4.1
IITM-RegCM4	IPSL-CMSA-LR	Institut Pierre-Simon Laplace (IPSL), France	IPSL	Dry	1.6	3.8

933

934

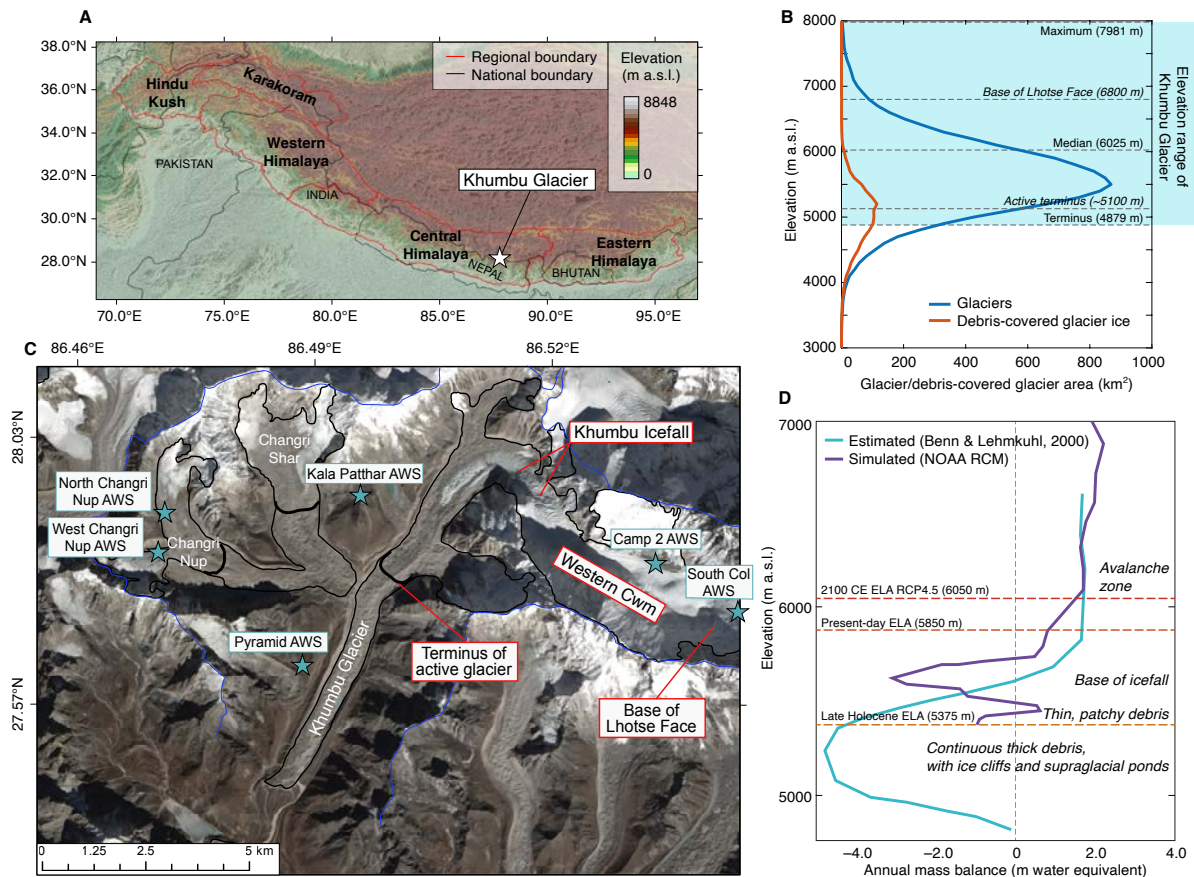
935 Table 2: COSIPY model parameters, where  $\alpha$  is albedo (of fresh snow, firn and ice),  $t^*$  decay time from  
 936 snow to firn,  $d^*$  the constant for the effect of snow depth on albedo, and  $z_0$  surface roughness length.

937

Parameter	Value	Unit	Source
$\alpha_{\text{freshsnow}}$	0.85	-	Mölg et al. 2012; Wagnon et al., 2009
$\alpha_{\text{firn}}$	0.6	-	Knap and Oerlemans, 1996; Mölg et al. 2012
$\alpha_{\text{ice}}$	0.3	-	Mölg et al. 2012
$t^*$	20	days	Mölg et al. 2012
$d^*$	1.0	cm	Mölg et al. 2012
$Z_{0\text{snow}}$	0.24	mm	Gromke et al., 2011
$Z_{0\text{firn}}$	4.0	mm	Brock et al., 2006
$Z_{0\text{ice}}$	1.7	mm	Brock et al., 2006
$Z_0$ ageing length (linearly from $Z_{0\text{snow}}$ to $Z_{0\text{firn}}$ )	60	days	Mölg et al. 2012

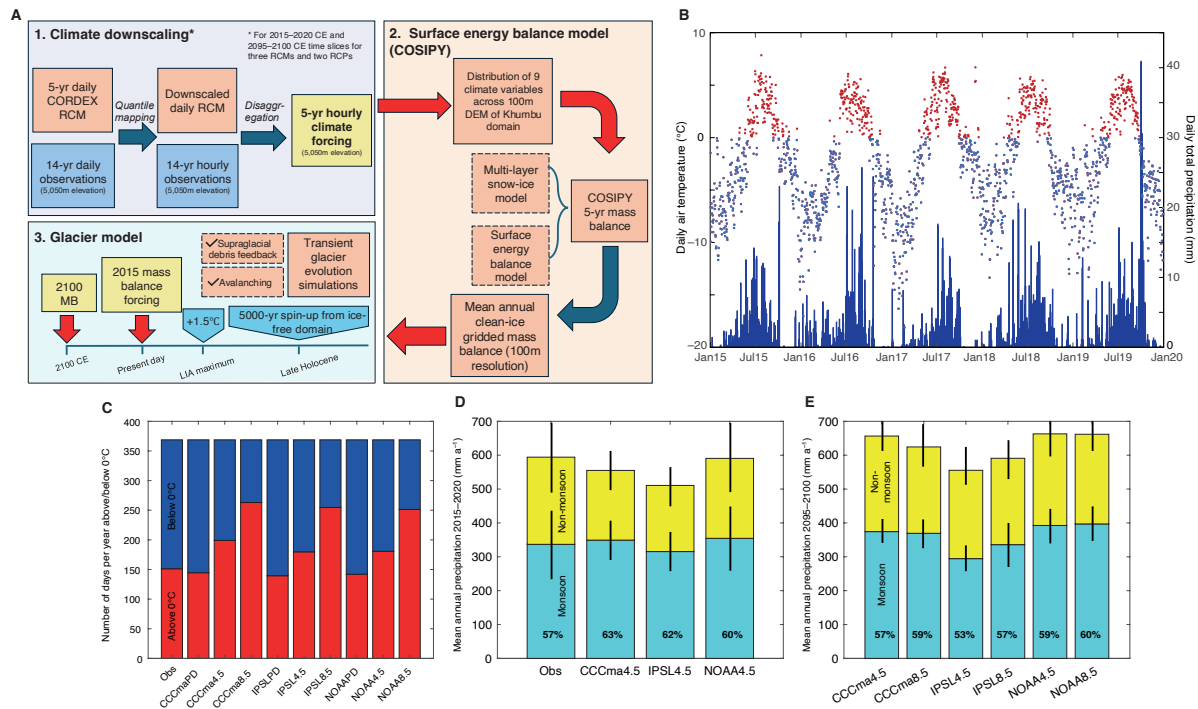
938

939 Figures and captions  
 940



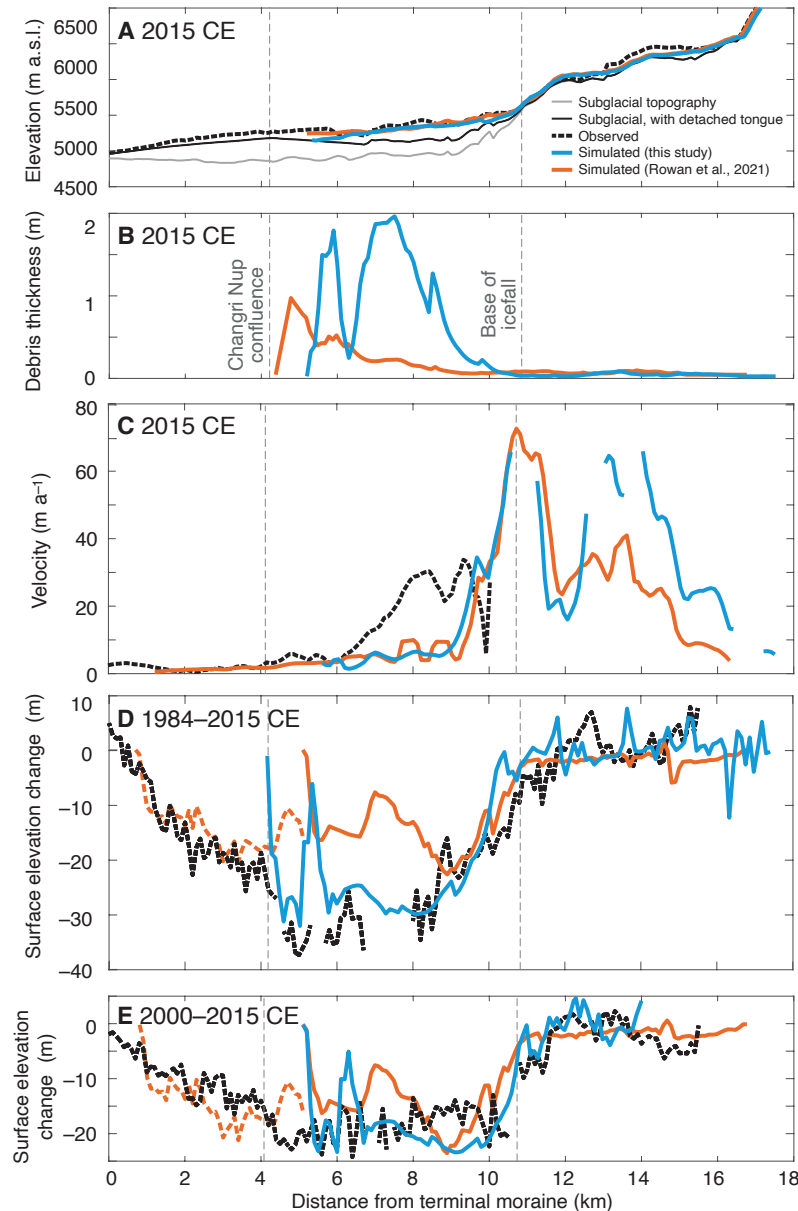
941  
 942  
 943 Figure 1: Khumbu Glacier location and context. (a) Map of High Mountain Asia showing the location of the  
 944 monsoon-influenced Central and Eastern Himalaya and Khumbu Glacier. (b) hypsometry of glaciers and  
 945 debris-covered glacier ice in the Central and Eastern Himalaya compared with the elevation range of  
 946 Khumbu Glacier. (c) Map of Khumbu Glacier showing the glacier outline from the RGI database (black line)  
 947 that is equivalent to the late Holocene (~1 ka) glacier extent identified from ice-marginal moraines, the  
 948 hydrological catchment that represents the model domain (blue line), the extent of supraglacial debris,  
 949 location of the Khumbu Icefall, the extent of active ice flow inferred from observations of glacier velocity,  
 950 and location of the automatic weather stations (AWS) used for RCM downscaling (blue stars). (d) Estimated  
 951 mass balance gradient for debris-covered glaciers in the Everest region (Benn and Lehmkühl, 2000)  
 952 compared with the glacier mass balance gradient simulated using the NOAA RCM, and showing change in  
 953 the equilibrium line altitude (ELA) of Khumbu Glacier in the historical and future simulations for the NOAA  
 954 RCM RCP4.5 experiment.

955  
 956  
 957  
 958



959  
 960  
 961  
 962  
 963  
 964  
 965  
 966  
 967  
 968  
 969  
 970  
 971  
 972  
 973  
 974  
 975  
 976  
 977  
 978  
 979  
 980  
 981

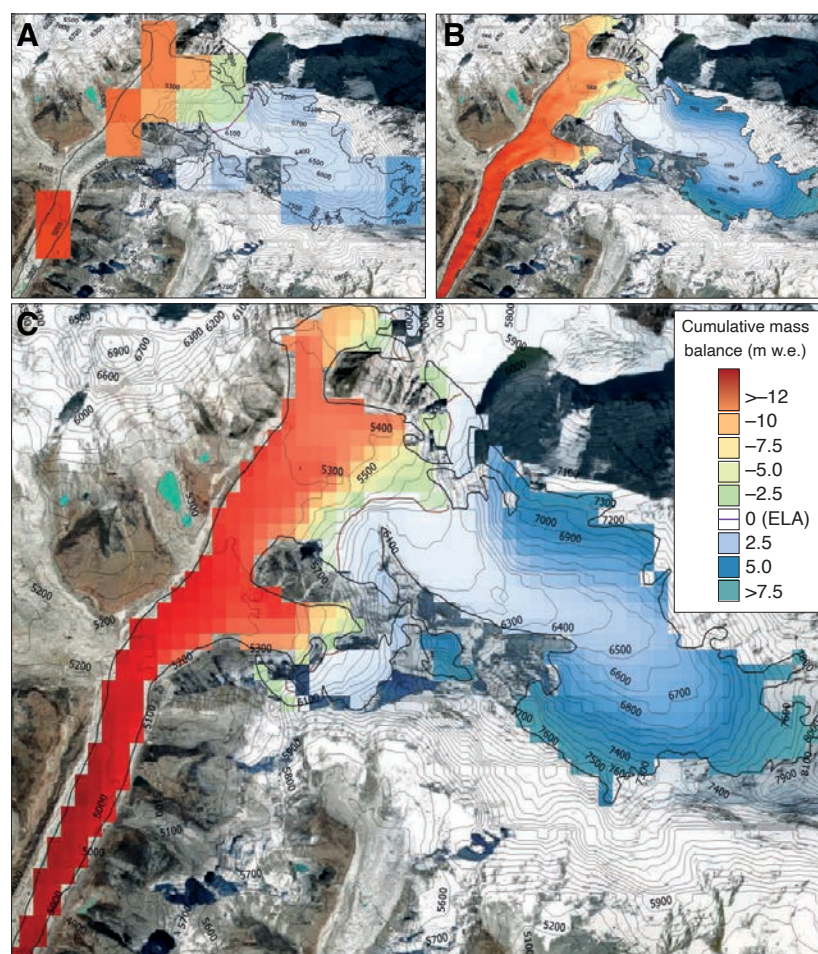
Figure 2: Glacier model experimental design and evaluation of RCM downscaling. (a) Schematic diagram of the glacier modelling approach showing the methods used for downscaling through quantile mapping and disaggregation of climate data. Surface energy balance modelling using COSIPY includes the preprocessing stage of meteorological distribution across the Khumbu domain, which is repeated for each RCM in the 2015–2020 CE climates and for the three RCMs and two RCPs for the 2095–2100 CE climates. The simulated mass balances are then used to force the iSOSIA model. (b) Daily mean temperature and daily total precipitation from the NOAA RCM for the present day (2015–2020 CE) following downscaling using quantile mapping with air temperature categorised into above freezing (red) and below freezing (blue). (c) Proportion of air temperatures above and below freezing for the present day for each RCM and RCP for the downscaled daily data compared with observations. (d) Annual precipitation totals for non-monsoon and monsoon with standard deviation between selected years shown by black bars for the downscaled daily data compared with observations. (e) Future (2095–2100 CE) time-slice annual precipitation totals for non-monsoon and monsoon months with standard deviation between selected years shown by black bars. In (d) and (e) the percentage of the total annual precipitation occurring during the monsoon is indicated by the value in bold text. (Obs = meteorological observations from AWS).



982  
983

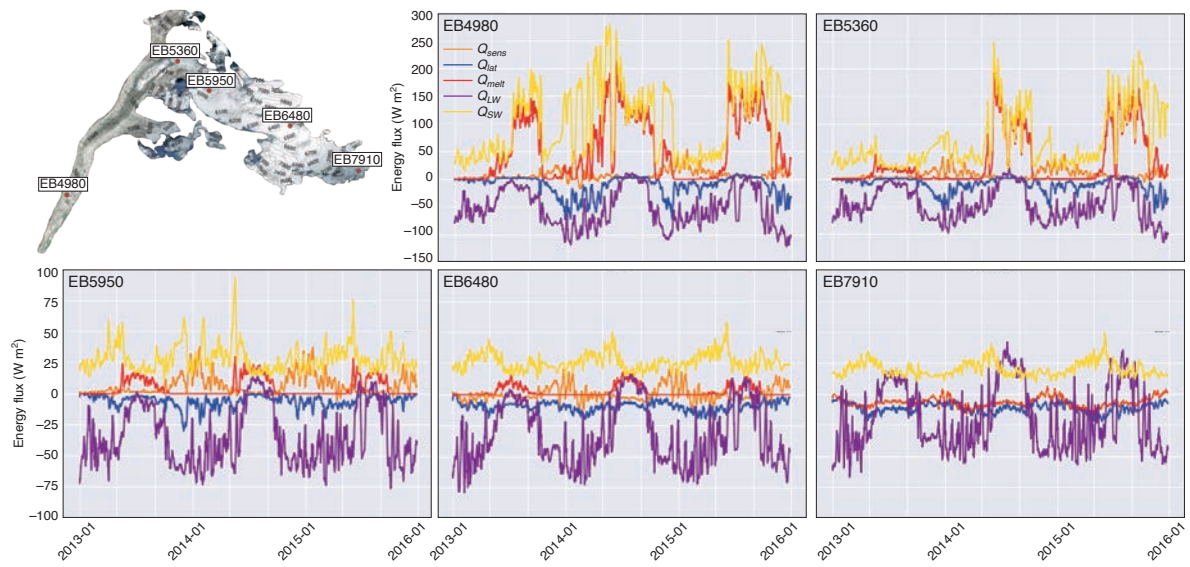
984 Evaluation of NOAA present-day simulation showing; (a) mean simulated glacier surface elevation and  
985 bed elevation calculated from a 500 m-wide swath profile along the central flowline of the glacier. and  
986 subglacial topography used in the entire glacier simulations in Rowan et al. (2015) was calculated by  
987 subtracting the ice thickness estimate (Farinotti et al., 2019) from the DEM, which represents an  
988 equivalent period. Subglacial topography including the dynamically detached debris-covered tongue  
989 added the simulated detached tongue to the initial subglacial topography, as described in Sect. 2.1. (b)  
990 mean simulated debris thickness, (c) simulated and observed velocities from the NASA MEaSUREs  
991 ITS\_LIVE project (Dehecq et al., 2019), and simulated and observed mean surface elevation change  
992 between (d) 1984–2015 CE and (e) 2000–2015 CE using geodetic observations from King et al. (2020)  
993 compared with results from the simulations in this study and those in Rowan et al. (2021) where further  
994 information about the model evaluation can be found.

995  
996  
997



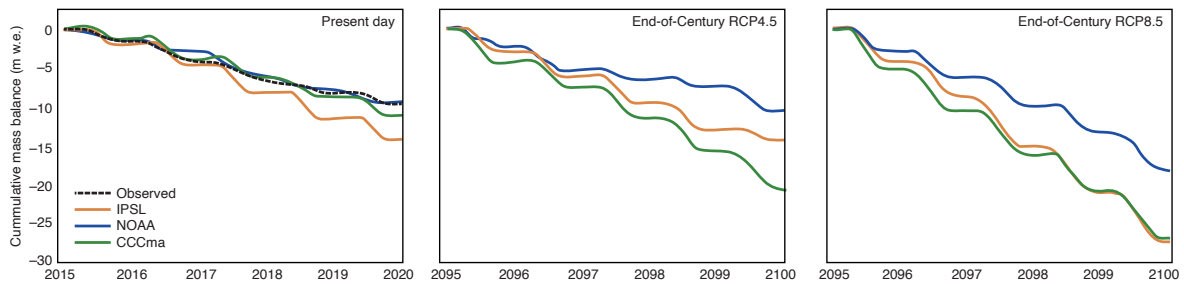
998  
999  
1000  
1001  
1002  
1003  
1004  
1005  
1006  
1007  
1008  
1009

Figure 4. COSIPY reference calculation of present-day mass balance for Khumbu Glacier for the period 2013–2015 CE showing the results from calculations using different grid spacings using (a) a 1-km grid, (b) a 30-m grid, (c) the 200-m grid spacing used throughout the experiments in this study.



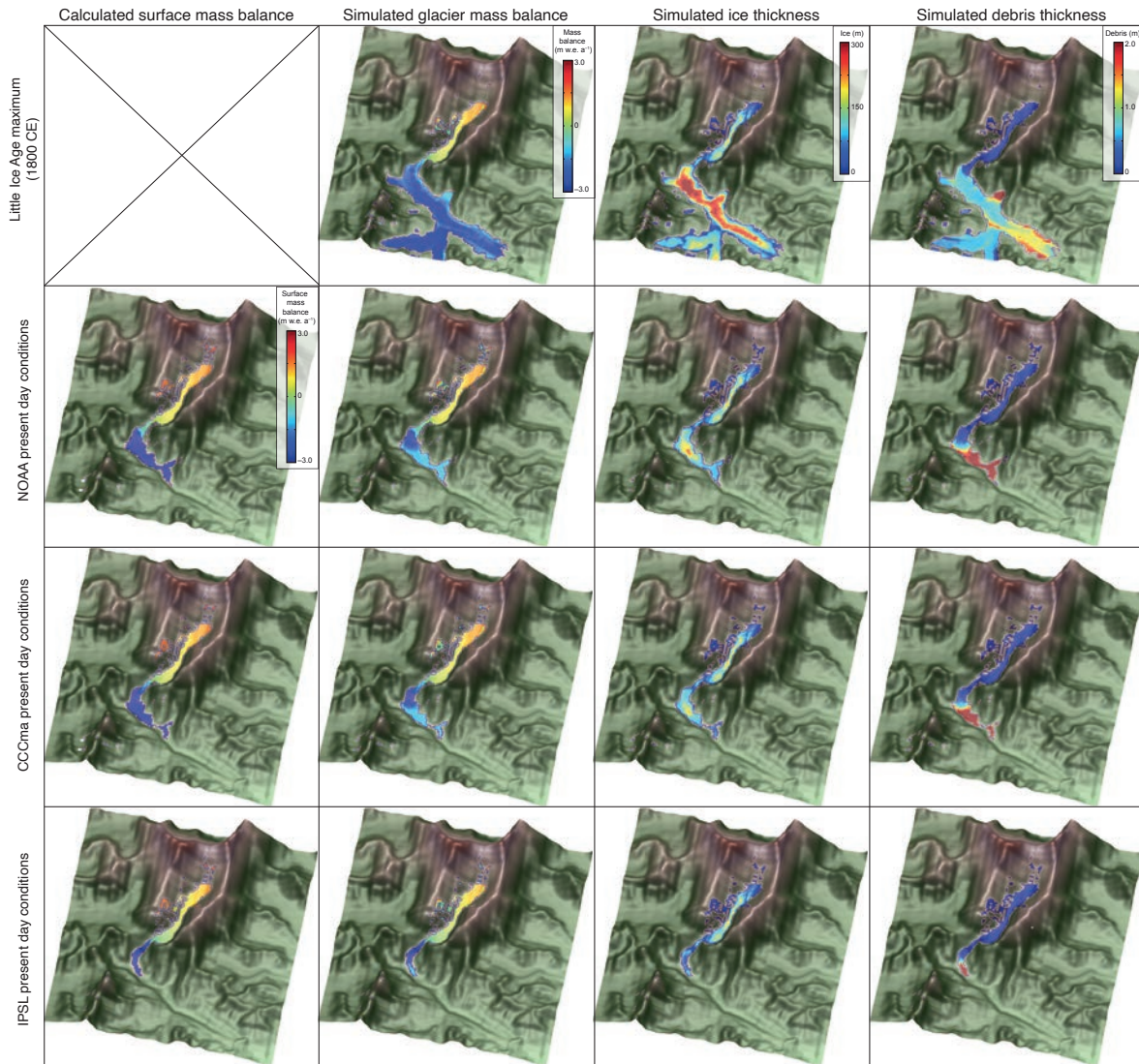
1010  
 1011  
 1012  
 1013  
 1014  
 1015  
 1016  
 1017  
 1018  
 1019  
 1020  
 1021

Figure 5. Locations of energy balance calculation points used for energy flux and melt components analysis in the reference calculation and sensitivity tests (named after their corresponding altitude e.g., EB6480) showing 5-day average of energy fluxes across study period for each site. Note that scales for energy flux are different for the two sites below the icefall compared to the three sites above the icefall.



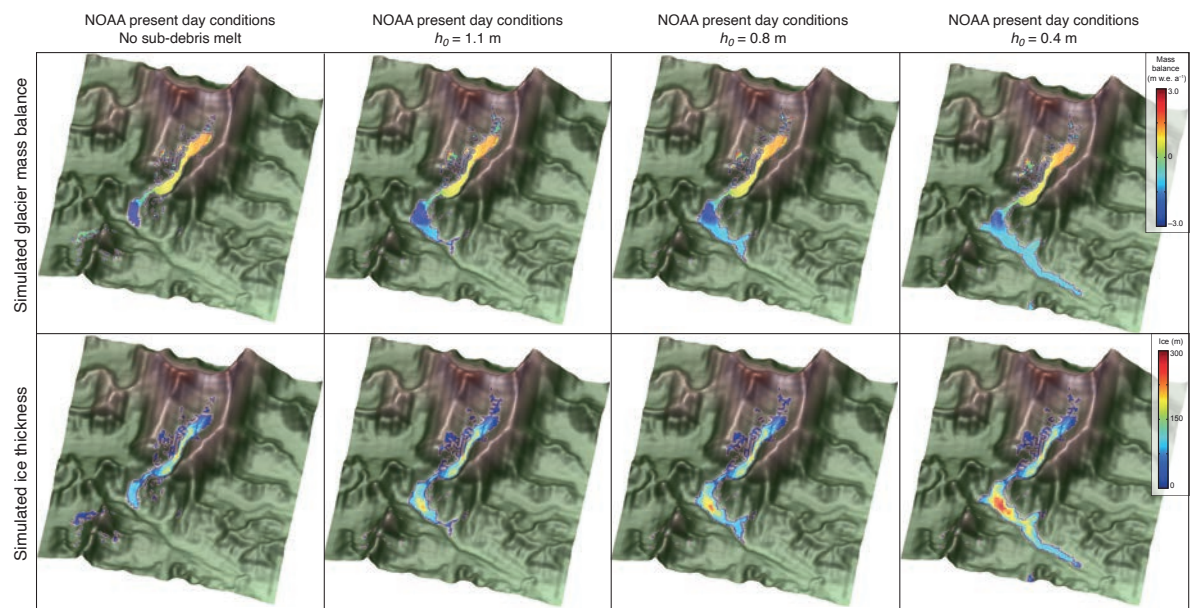
1022  
 1023  
 1024  
 1025  
 1026  
 1027  
 1028  
 1029  
 1030  
 1031  
 1032

Figure 6. Spatially averaged cumulative clean-ice mass balance with clear seasonality for the present day time slice including the mass balance forced by the observations used for downscaling, and the end-of-Century time slice under RCP4.5 and RCP8.5. The low annual glacier-wide mass balance values shown here result from the extent of the model domain used to force the glacier model that includes the larger catchment beyond the glacier margins and therefore contains a higher proportion of lower elevations than those of the glacier itself. However the similarity between the mass balance results for simulations forced by NOAA RCM and observations can be clearly seen, and the differences between the three RCMs is apparent in all time slices.



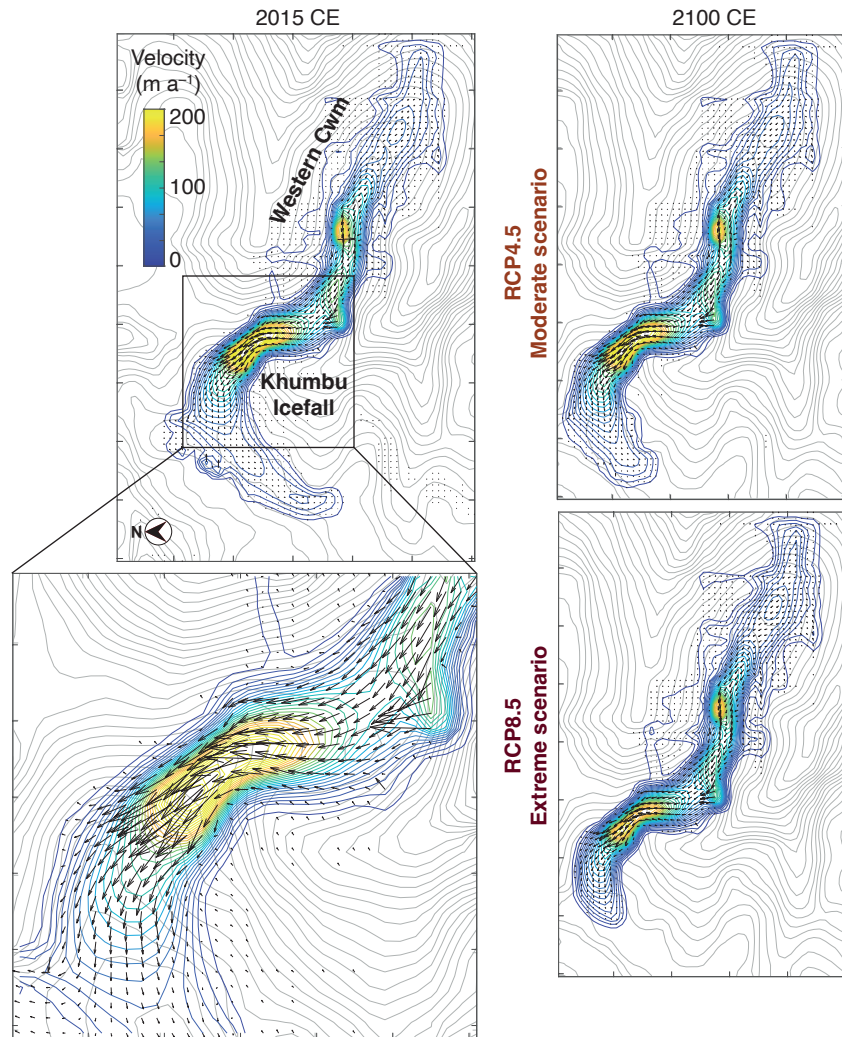
1033  
 1034  
 1035  
 1036  
 1037  
 1038  
 1039  
 1040  
 1041

Figure 7. iSOSIA model sensitivity to surface energy and mass balance forcing, showing ‘Little Ice Age’ (~1800 CE) maximum glacier mass balance, ice thickness and debris thickness. Present-day results for surface mass balance calculated using each RCM with COSIPY showing glacier mass balance calculated using the same climate forcing following integration with the glacier model, simulated ice thickness, and simulated debris thickness.



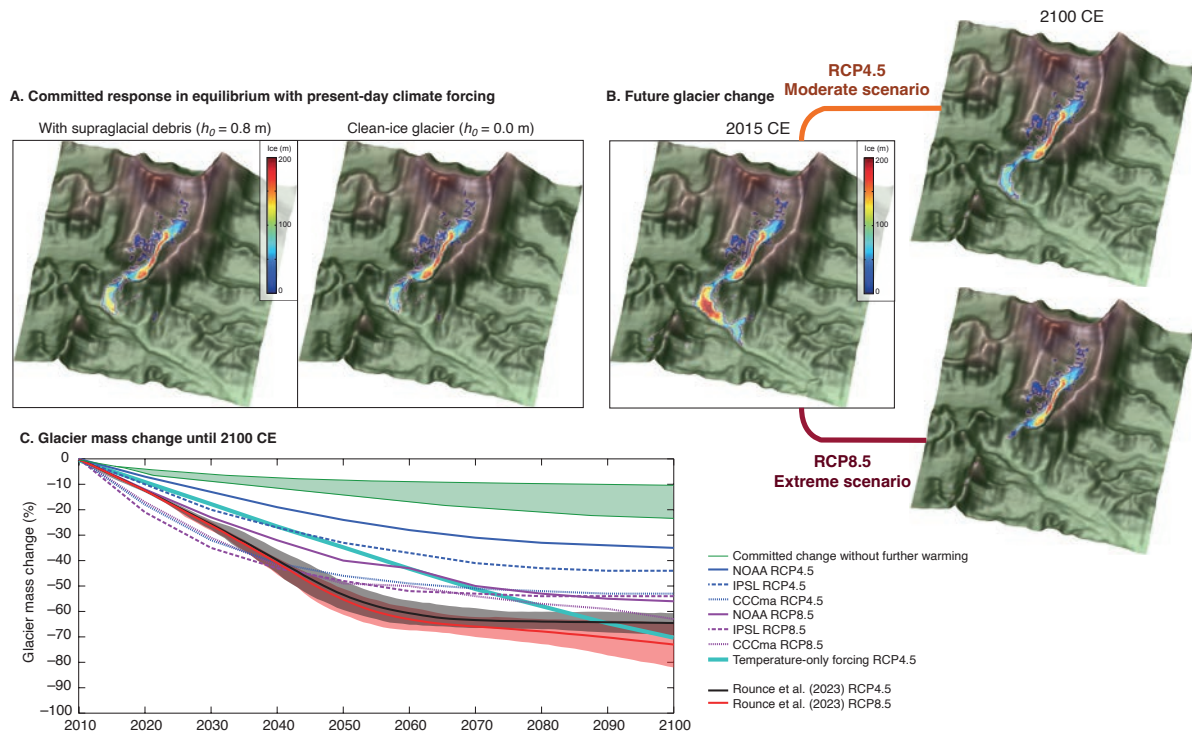
1042  
1043  
1044  
1045  
1046  
1047  
1048  
1049  
1050  
1051  
1052

Figure 8. Glacier mass balance and ice thickness simulated using the NOAA RCM climate forcing and the resulting simulated ice thickness where no sub-debris melt is imposed and the glacier has an entirely debris-free surface compared with ice results for simulations with  $h_0$  values of 0.4 m, 0.8 m, and 1.1 m where  $h_0$  is a constant in Equation (1) representing the characteristic debris thickness at which the reduction in ablation due to insulation by supraglacial debris is 50% of the value for an equivalent clean-ice surface (Anderson and Anderson, 2016; Rowan et al., 2021) .



1053  
1054  
1055  
1056  
1057  
1058  
1059  
1060  
1061  
1062  
1063  
1064

Figure 9. Simulated ice flow for Khumbu Glacier. Velocity-vector maps showing simulated ice flow magnitude and direction from the present day (2015–2020 CE) and 2100 CE under RCP4.5 and RCP8.5 using the downscaled NOAA climate forcing. Simulated ice flow speed is shown as colour shading with blue contours, and the bed topography is shown by grey contours. The outermost contour in each plot represents the slowest ice flow close to the glacier margins with depth-integrated velocities of 5–10 m a<sup>-1</sup>. Note that rapid flow across the Western Cwm indicated by a single arrow represents the effects of avalanching rather than sustained glacier flow.



1065  
 1066  
 1067  
 1068  
 1069  
 1070  
 1071  
 1072  
 1073  
 1074  
 1075  
 1076  
 1077  
 1078

Figure 10. Future glacier volume change projections until 2100 CE. (a) Equilibrium ice thickness accounting for the committed response to recent climate change using the downscaled NOAA RCM climate forcing with and without the effect of supraglacial debris on mass balance. (b) Simulated ice thickness under RCP4.5 and RCP8.5 for 2100 CE using the downscaled NOAA RCM climate forcing. (c) Comparison of projected shrinkage of Khumbu Glacier by 2100 CE from this study with those from Rounce et al. (2023) showing results from each of the six experiments in this study with results from RCP4.5 and RCP8.5 from Rounce et al. (2023), the equivalent result for a simulation using a change in MAAT equivalent to the NOAA RCP4.5 forcing where precipitation does not change from the present-day value (cyan line). The green shading shows the range of the committed volume loss due to historical warming.

1079 **Appendix**

1080 This appendix contains further details on the meteorological data collection and analysis, RCM  
1081 downscaling, evaluation of the present-day downscaled RCM results using meteorological data and the  
1082 distribution of these results across the model domain, and the parameterisation and sensitivity testing  
1083 of the COSIPY model. The Indian Summer Monsoon season was defined as June to October, the post-  
1084 monsoon as October–November, winter as December–February, and the pre-monsoon as March–May  
1085 (Ueno et al., 2008). Although much of this study compares the monsoon season against the non-  
1086 monsoon season, it should be noted that the timing of monsoon onset and cessation can vary between  
1087 years. Day time was defined as 08:00–16:00 and night as 20:00–04:00 (Nepal local time) to account for  
1088 changing sunrise and sunset times throughout the year and the influence of topographic shading in the  
1089 valleys; centred-means were used for some datasets to remove local noise associated with daily  
1090 frequencies. For sub-hourly measurements, hourly averages were calculated using data from the  
1091 previous hour. The period for the reference simulation and sensitivity experiments was January 1<sup>st</sup> 2013  
1092 to December 31<sup>st</sup> 2015. RCM downscaling to produce the five-year time slices represented the periods  
1093 January 1<sup>st</sup> 2015 to December 31<sup>st</sup> 2019 and January 1<sup>st</sup> 2095 to December 31<sup>st</sup> 2099.  
1094

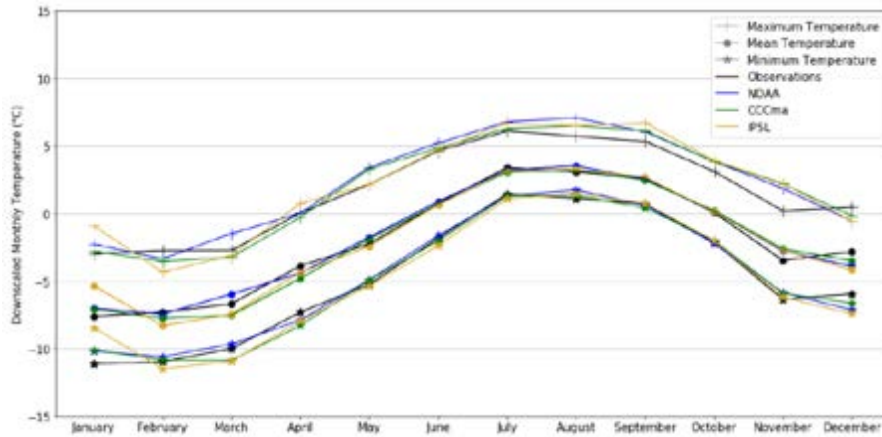
1095 **A1. Gap filling of the AWS data**

1096 All AWS datasets contained periods of erroneous measurements and missing data, which is unsurprising  
1097 given the challenges of maintaining equipment in such an environment (Oulkar et al., 2026). Daily air  
1098 temperature averages were calculated when 83% (20 hours) of observations were available. For  
1099 calculation of lapse rates for longer time periods (e.g. daytimes during the monsoon season) the  
1100 distributions of missing data across these periods were analysed. For example, the Lukla AWS had  
1101 almost 45% of temperature observations missing during the monsoon season but as these were equally  
1102 distributed between day and night, lapse rates could be calculated using station pairs following the  
1103 method of Immerzeel et al. (2014). Up to 13% of the West Changri Nup AWS temperature records were  
1104 missing, and these were interpolated using the Ev-K2-CNR Pyramid AWS data with the same lapse rate  
1105 as the GlacioClim dataset. The interpolated results were compared with the preceding and succeeding  
1106 periods from the same AWS, and the preceding and succeeding months from other AWS, and compared  
1107 with data collected in November 2014 at the GlacioClim North Changri Nup AWS (5,470 m a.s.l.).  
1108

1109 Data gaps in the precipitation datasets were significant, particularly during the onset of the monsoon  
1110 (e.g., 45% of data points were missing for the Namche AWS) meaning the altitudinal dependency of  
1111 precipitation could not be fully characterised. This led to several monsoon seasons with little or no data  
1112 at individual AWS. Given that the aim of this study was to analyse *in situ* trends, gap-filling through  
1113 interpolation was not conducted for these AWS during the seasons without data. Station pairs were used  
1114 to determine the elevation dependency of precipitation for the reference simulation following the  
1115 method of Immerzeel et al. (2014). Results from the Kala Patthar/Pheriche station pair and the  
1116 Pyramid/Pheriche station pair in 2009, and the Kala Patthar/Namche station pair during 2011, show that  
1117 the relationship between precipitation amount and elevation was more negative during the monsoon  
1118 season ( $-0.011\% \text{ m}^{-1}$  to  $-0.018\% \text{ m}^{-1}$ ) than during the non-monsoon ( $-0.0039\% \text{ m}^{-1}$  to  $-0.0043\% \text{ m}^{-1}$ ).  
1119 No interpolation to fill data gaps was required for other meteorological variables, apart from albedo  
1120 but as this was only measured at the West Changri Nup AWS there was no suitable surrogate for this  
1121 variable.  
1122

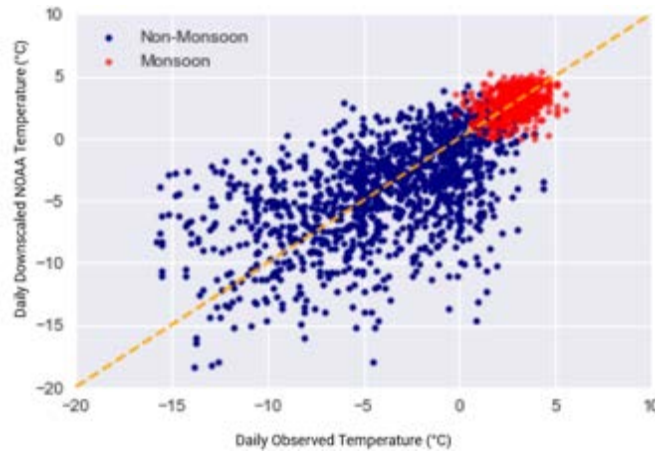
1123 **A2. Downscaled climate model results compared with observations**

1124  
1125



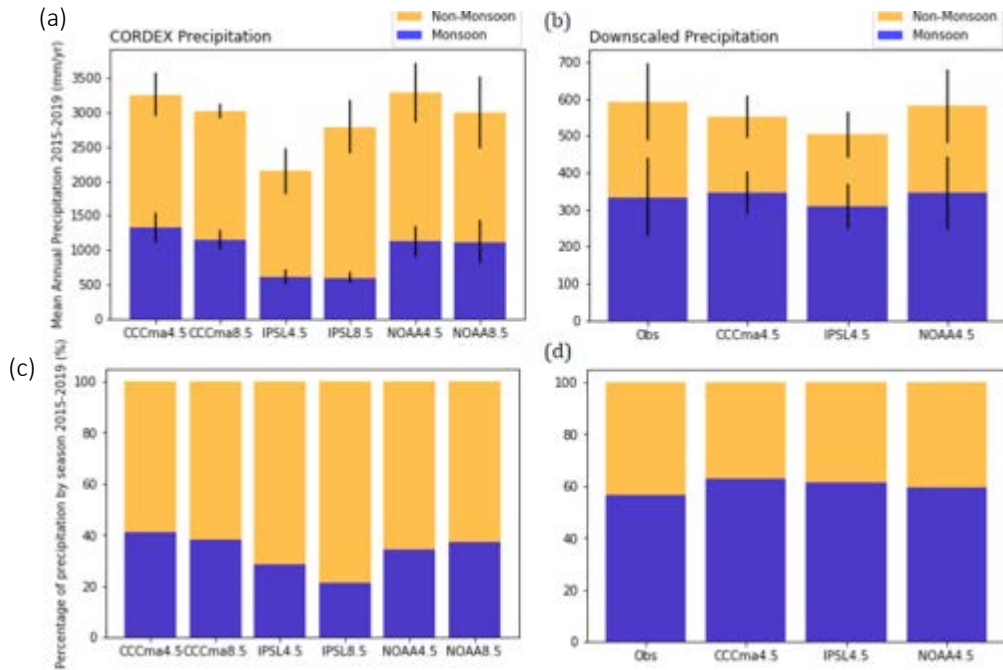
1126  
1127  
1128  
1129  
1130  
1131  
1132  
1133  
1134

Figure A1: Downscaled monthly mean, maximum, and minimum temperature calculated for the present day time slice compared with observations from the GlacioClim Pyramid Observatory AWS.



1135  
1136  
1137  
1138  
1139  
1140  
1141  
1142  
1143

Figure A2: Daily downscaled temperature from the NOAA RCM against observations from the GlacioClim Pyramid Observatory AWS split by monsoon/non-monsoon. The 1:1 relationship is shown by the dashed orange line.

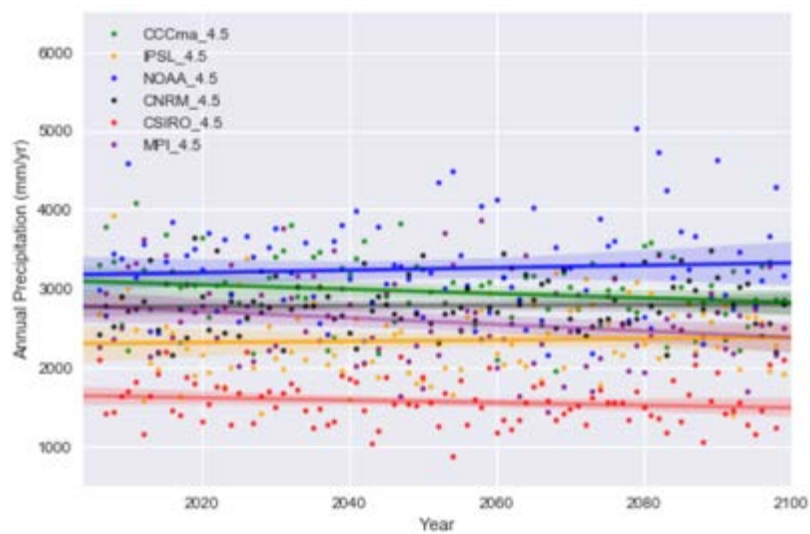


1144  
 1145  
 1146  
 1147  
 1148  
 1149  
 1150  
 1151  
 1152  
 1153  
 1154  
 1155  
 1156  
 1157  
 1158  
 1159

Figure A3. Annual precipitation totals for the monsoon and non-monsoon seasons. (a and b) Precipitation totals before and after downscaling, with the standard deviation between selected years shown by black bars. (c and d) The same results as seasonal percentages. The annual precipitation is in good agreement with measurements in the southern Dudh Koshi catchment for the gridbox nearest to Khumbu Glacier is located at 27.9065056°N, 86.4352951°E at 2,100 m a.s.l..

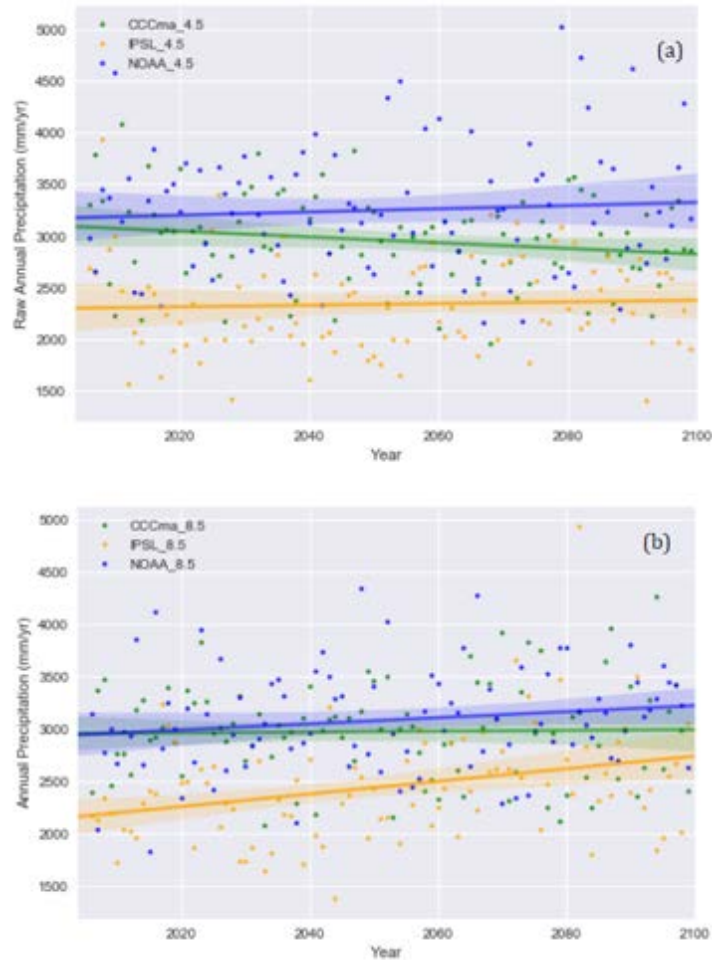
### A3. Regional Climate Model analysis and selection

Three of the six available CORDEX South Asia RCMs (NOAA, CCCma, IPSL) were selected as discrete scenarios that spanned the range of possible future precipitation conditions (Table 1); either wet, moderate, or dry climate in 2080–2100 CE (Fig. A4). The raw RCMs significantly overestimated the annual total precipitation by at least a factor of five for the selected gridpoint, which was corrected by downscaling of these results using the AWS data.



1160  
 1161  
 1162  
 1163  
 1164

Figure A4: Annual precipitation sums (dots) with fitted trend line from the start of the RCP experiments (2006–2100 CE) for each of the six Indian Institute for Tropical Meteorology CORDEX models for RCP4.5.



1165  
1166  
1167  
1168  
1169  
1170  
1171  
1172  
1173  
1174  
1175  
1176  
1177  
1178  
1179  
1180  
1181  
1182  
1183  
1184  
1185  
1186  
1187  
1188  
1189  
1190  
1191  
1192

Figure A5: Annual precipitation sums (dots) with fitted trend line from the start of the RCP experiments (2006–2100 CE) for the three selected of the six CORDEX models for (a) RCP4.5 and (b) RCP8.5.

#### A4. Downscaling parameters and method

While minimum and maximum air temperatures are not required to as inputs to COSIPY, these were downloaded and statistically downscaled using quantile mapping with normal distribution to aid disaggregation to an hourly time step using MELODIST (Table A1). Quantile mapping for the CORDEX wind speed data was found to be ineffective when analysing the time series output against observations, both for the absolute wind speed as well as the reduced day-on-day variability seen during the monsoon season, and therefore, GARD was used instead. This is a simple statistical analogue regression downscaling method appropriate for pointwise downscaling.

1193

Table A1: RCM-derived parameters and the method used for downscaling or bias correction.

RCM-derived parameters	Downscaling/bias correction method	Parametric distribution model (for Quantile mapping)	References
Precipitation (kg per m <sup>2</sup> per s, converted to mm day <sup>-1</sup> )	Quantile mapping	Gamma	Vrac et al., 2007; Piani et al., 2010
Mean temperature (K) Minimum temperature (K) Maximum temperature (K)	Quantile mapping	Normal / Gaussian	Li et al., 2010, Gupta et al., 2016; Luo et al., 2018
Incoming shortwave (W m <sup>-2</sup> ) Incoming longwave (W m <sup>-2</sup> ) Relative humidity (%)	Quantile mapping	Beta	Ruane et al., 2015
Pressure (hPa)	Bias correction	Not applicable	Not applicable
Wind speed (m s <sup>-1</sup> )	Regression downscaling	Not applicable	Gutmann et al., 2022

1194

1195

1196

### A5. Variability in surface energy balance with elevation

1197

1198

1199

1200

1201

1202

1203

1204

1205

1206

1207

1208

1209

The contributions of the components of the surface energy balance were tested at five points along the glacier centreline (Fig. 5) and found to vary substantially in both absolute values and seasonality. Net shortwave radiation ( $Q_{SW}$ ) contributed the largest energy input to the glacier surface at the lower elevation sites and correlated most strongly with  $Q_{melt}$ . The high temporal variability related to varied cloud cover and fluctuating albedo during the warmer months with the melting of the snowpack.  $Q_{SW}$  was low at higher elevations, but high  $SW_{in}$  at the higher sites indicates that this is not due to topographic shading.  $Q_{SW}$  is correlated with albedo, and the persistence of snow throughout much of the year will reduce  $Q_{melt}$ .  $Q_{LW}$  rose above zero during the monsoon season at sites EB5950, EB6480 and EB7910, mostly due to heavy cloud cover and increased temperatures relative to the glacier surface.  $Q_{lat}$  was close to zero at the lower elevation sites as the arrival of the monsoon led to higher relative humidity, and this pattern was similar but dampened at higher elevations. At the highest site, EB7910,  $Q_{melt}$  correlated exactly with the sensible heat flux.

1210

1211

1212

1213

1214

1215

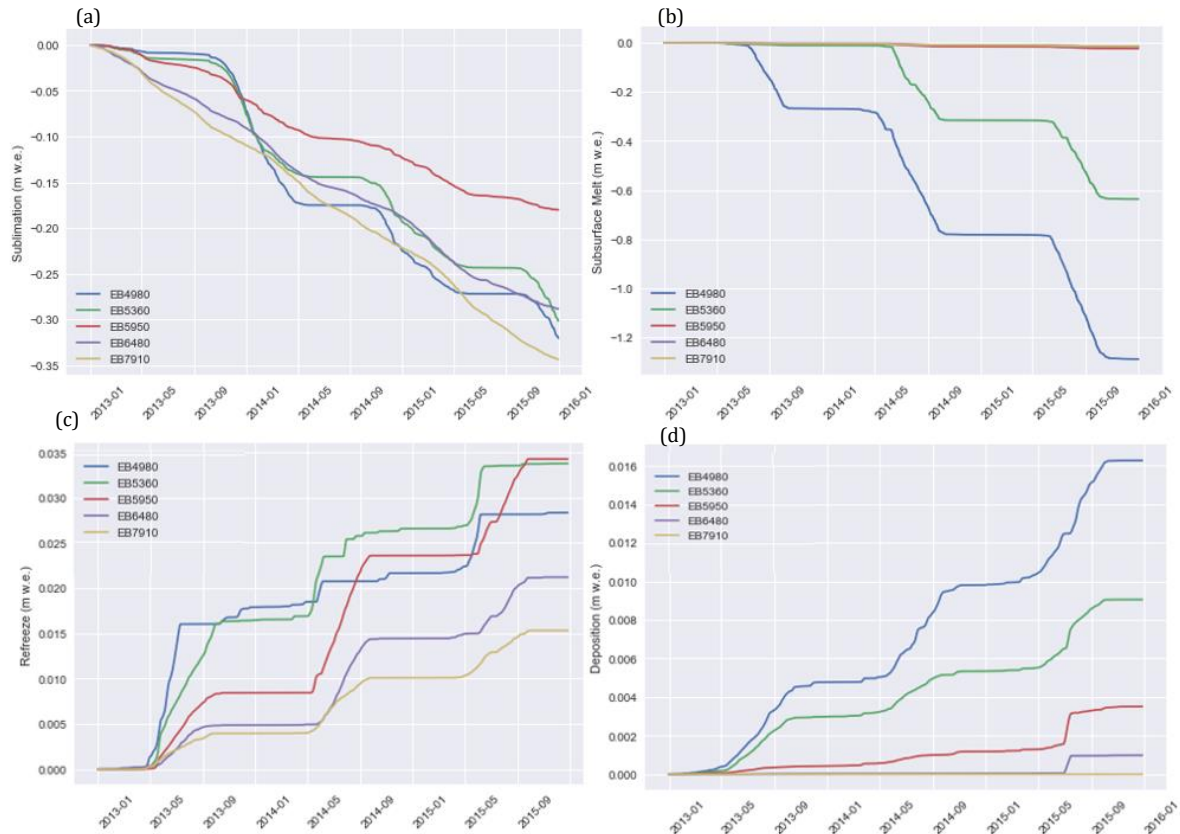
1216

1217

1218

1219

Sublimation occurred at all elevations, with the highest cumulative loss at EB7910 (Fig. A6A). Sublimation rates correlated with seasonality down-glacier; at EB7910 sublimation only slightly slowed from December until May, while sublimation at site EB4980 increased from April until the start of the monsoon in July. Subsurface melt at or above the ELA (5,950 m a.s.l.) was negligible, but lower elevation sites showed stronger seasonal cycles related to surface temperatures. Refreezing (Fig. A6C) occurred at all sites and the onset of refreezing was staggered with increasing elevation, although absolute values remained low. Higher  $Q_{lat}$  during the monsoon resulted in higher deposition of snow to the glacier at lower elevations and negligible rates at higher elevations. Similar absolute values and patterns are seen for condensation (results not shown).



1220  
 1221  
 1222  
 1223  
 1224  
 1225  
 1226

Figure A6. 5-day averages of (a) sublimation, (b) subsurface melt, (c) refreeze, and (d) deposition for the five surface energy balance sensitivity testing sites across Khumbu Glacier (see Fig. 5 for locations of these sites).

### A6. COSIPY parameter testing and sensitivity results

1228 To isolate the impact of individual surface energy balance variables on the mass balance of Khumbu  
 1229 Glacier, each variable was perturbed individually, and air temperature and precipitation amount were  
 1230 tested in tandem for the reference period 2013–2015 CE (Table A2). Perturbations of all variables were  
 1231 within the range of possible uncertainty that arise from a combination of observations, climate models,  
 1232 downscaling approach or the distribution of meteorology. The positive temperature and precipitation  
 1233 perturbations were in the order of possible future climate forcings. The spatially averaged mass balance  
 1234 was most sensitive to changes in  $LW_{in}$ , air temperature, and  $SW_{in}$ , and relative humidity had the least  
 1235 impact on ablation/accumulation rates (Fig. A7). The coupled parameter testing (Fig. A8) perturbed  
 1236 precipitation and air temperature simultaneously. The most significant change in spatially averaged  
 1237 mass balance followed a 3°C increase in air temperature and 20% decrease in precipitation amount. The  
 1238 increase in ablation following an increase in air temperature of 1.5°C was completely compensated by  
 1239 the increase in accumulation resulting from a 20% increase in precipitation amount.

1240  
 1241 Accurate estimation of precipitation phase is important for summer-accumulation type glaciers and  
 1242 threshold values of air temperature are often used to separate liquid and solid precipitation. Previous  
 1243 work calculated threshold temperatures across 6,883 AWS in the Northern Hemisphere to find an  
 1244 average rain/snow partitioning value of 1°C, with 95% of observations falling between 0.4°C and 2.4°C  
 1245 (Jennings et al., 2018). Although there remains a lack of such data for High Mountain Asia, Jennings et  
 1246 al. (2018) found that high mountain areas have the highest rain/snow partitioning thresholds, with a  
 1247 value of up to 4.5°C on the Tibetan Plateau. The impact of two different precipitation partitioning  
 1248 schemes on glacier mass balance was investigated here. Threshold temperatures of 0.5°C, 2.0°C and

1249 3.5°C were chosen and compared with the default value in COSIPY (STF), and a scheme that smoothly  
 1250 scaled from 100% solid precipitation at -1°C to 0% solid precipitation at 4°C was also tested.

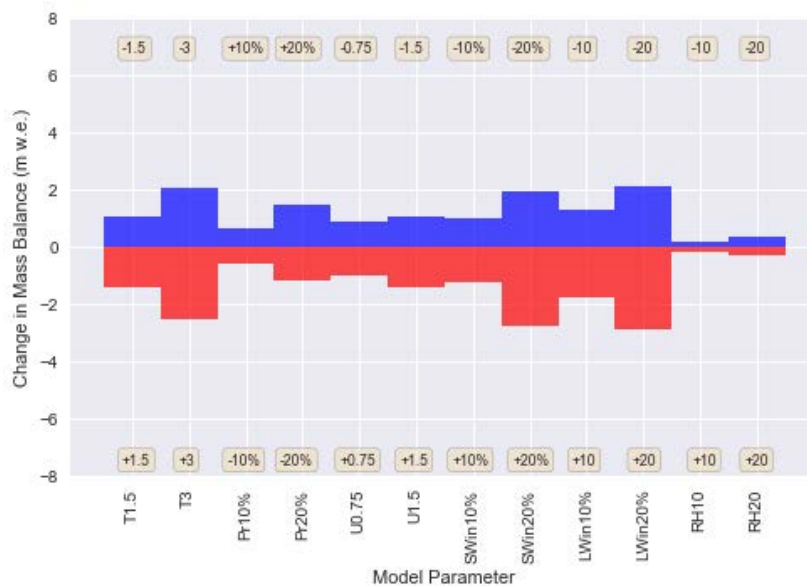
1251  
 1252 The glacier ice surface roughness ( $z_0$ ) was defined as 1.7 mm for the reference simulation, which is a  
 1253 reasonable estimate for clean-ice glaciers (Mölg et al., 2012). The  $z_0$  values reported within the literature  
 1254 vary widely for clean-ice glaciers, and two substantially different  $z_0$  values were tested. A  $z_0$  value of  
 1255 0.1 mm was measured at Midtre Lovénbreen, Svalbard (Irvine-Fynn et al. 2014), and August-One  
 1256 glacier, China (Guo et al., 2018), and a  $z_0$  value of 6.9 mm was calculated on the clean-ice section of  
 1257 the Haut Glacier D’Arolla (Brock et al., 2006) and Laohugou Glacier No. 12 (Sun et al., 2018). These  
 1258 values were used as endmembers of the likely range in values for Khumbu Glacier. The  $z_0$  value had  
 1259 minimal impact on glacier mass balance (Fig. A9) although a higher (lower) value for  $z_0$  did result in  
 1260 slightly increased (decreased) mass balance. The mass balance sensitivity was not proportional to the  
 1261 change in  $z_0$ , with a  $z_0$  value of 1.6 mm lower than the reference value leading to a similar mass balance  
 1262 change than that of the experiment with a  $z_0$  value of 5.2 mm higher than the reference value.

1263  
 1264 The albedo values of the three glacier components were perturbed by  $\pm 0.05$  from that used in the  
 1265 reference experiment (e.g., 0.85 for fresh snow). There was a strong response of the glacier mass balance  
 1266 to changing snow albedo. Reducing snow albedo by 0.05 led to a 65% reduction in mass balance of  
 1267 2.21 m w.e. (Fig. A9). Ablation (accumulation) rates were 3.7 m w.e. (1.75 m w.e.) higher relative to  
 1268 the reference simulation for this perturbation. This result further supports the importance of  $Q_{SW}$  to  
 1269 ablation rates. Varying albedo values for firn and ice also revealed a lower sensitivity of glacier mass  
 1270 balance relative to snow albedo.

1271  
 1272  
 1273 Table A2. Parameter perturbations for the sensitivity experiments. Note that for relative humidity the %  
 1274 refers to the units and not the perturbation.  
 1275

Parameter	Perturbation
Mean annual air temperature (C)	$\pm 1.5, \pm 2.0, \pm 3.0$
Precipitation amount (%)	$\pm 10, \pm 20, \pm 30$
Wind speed ( $\text{m s}^{-1}$ )	$\pm 0.75, \pm 1.5$
$SW_{in}$ and $LW_{in}$ (%)	$\pm 10, \pm 20$
Relative Humidity (%)	$\pm 10, \pm 20$

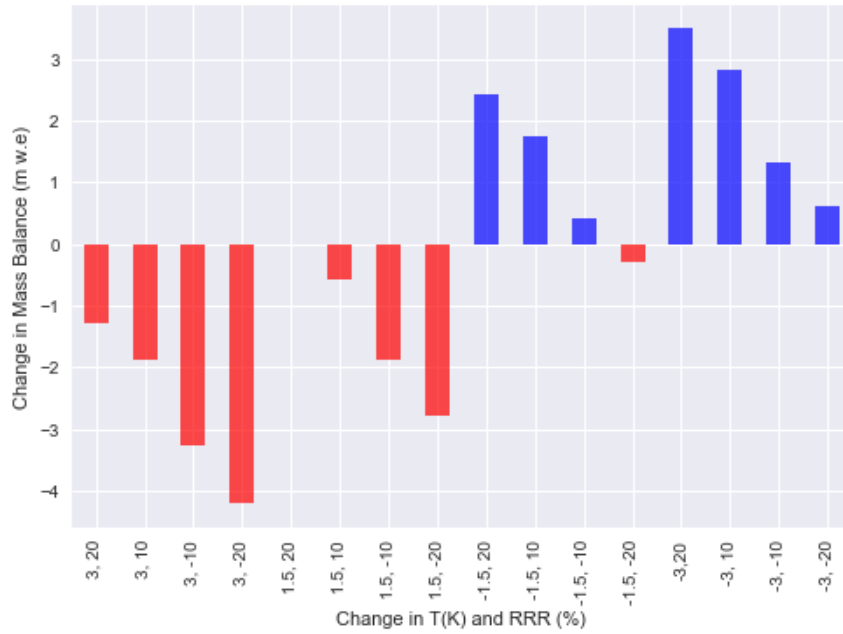
1276



1277

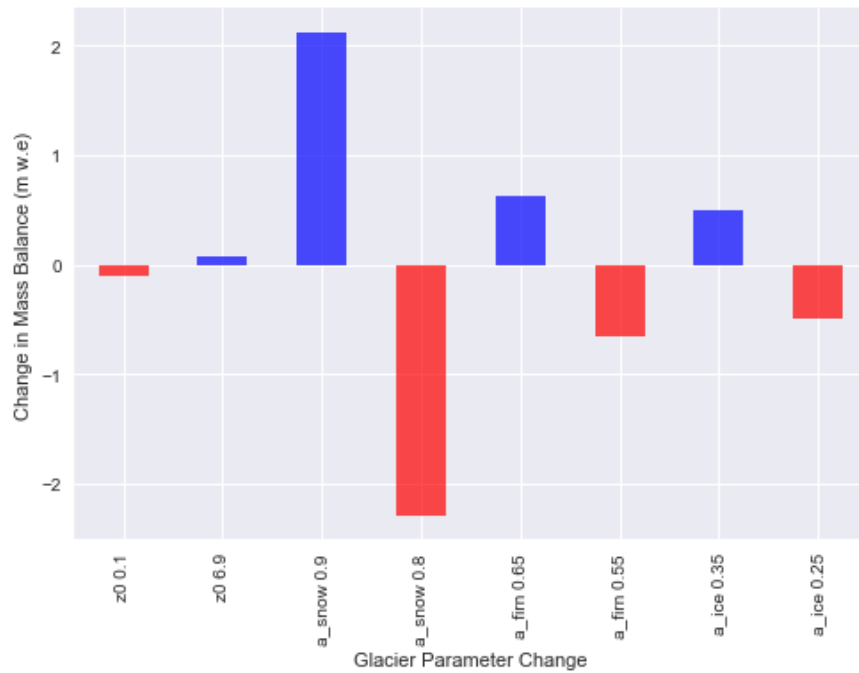
1278

1279 Figure A7. Single parameter sensitivity test results for reference simulation period 2013–2015 CE.



1280  
 1281  
 1282  
 1283  
 1284  
 1285  
 1286

Figure A8. Coupled parameter sensitivity test results for mean annual air temperature and precipitation amount for reference simulation period 2013–2015 CE.



1287  
 1288  
 1289  
 1290  
 1291  
 1292  
 1293  
 1294  
 1295  
 1296

Figure A9. Sensitivity of mass balance for the reference simulation period 2013–2015 CE to changing glacier parameters (surface roughness, and albedo of snow, firn, and ice).

1297 **References**

- 1298 Ageta, Y.: Characteristics of precipitation during monsoon season in Khumbu Himalaya, *Seppyo*, 38, 84–88,  
1299 [https://doi.org/10.5331/seppyo.38.Special\\_84](https://doi.org/10.5331/seppyo.38.Special_84) (last access: 18 May 2026), 1976.  
1300
- 1301 Altena, B. and Kääh, A.: Ensemble matching of repeat satellite images applied to measure fast-changing ice flow,  
1302 verified with mountain climber trajectories on Khumbu icefall, Mount Everest, *J. Glaciol.*, 66, 905–915,  
1303 <https://doi.org/10.1017/jog.2020.66>, 2020.  
1304
- 1305 Anderson, L. S. and Anderson, R. S.: Modeling debris-covered glaciers: response to steady debris deposition, *The*  
1306 *Cryosphere*, 10, 1105–1124, <https://doi.org/10.5194/tc-10-1105-2016>, 2016.  
1307
- 1308 Arndt, A., Sauter, T., and Saß, B.: cryotools/cosipy: COSIPY v1.3 – An open-source coupled snowpack and ice  
1309 surface energy and mass balance model (v1.3), Zenodo [code], <https://doi.org/10.5281/zenodo.3902191>,  
1310 2020.  
1311
- 1312 Bartlett, O. T., Ng, F. S. L., and Rowan, A. V.: Morphology and evolution of supraglacial hummocks on debris-  
1313 covered Himalayan glaciers, *Earth Surf. Process. Landforms*, 46, 525–539,  
1314 <https://doi.org/10.1002/esp.5043>, 2021.  
1315
- 1316 Benn, D. I. and Lehmkuhl, F.: Mass balance and equilibrium-line altitudes of glaciers in high-mountain  
1317 environments, *Quatern. Int.*, 65–66, 15–29, [https://doi.org/10.1016/S1040-6182\(99\)00034-8](https://doi.org/10.1016/S1040-6182(99)00034-8), 2000.  
1318
- 1319 Benn, D. I. and Owen, L. A.: The role of the Indian summer monsoon and the mid-latitude westerlies in Himalayan  
1320 glaciation: review and speculative discussion, *Journal of the Geological Society*, 155, 353–363,  
1321 <https://doi.org/10.1144/gsjgs.155.2.0353>, 1998.  
1322
- 1323 Biemans, L. H., Speelman, F., Ludwig, E. J., Moors, A. J., Wiltshire, P., Kumar, D., Gerten, P., and Kabat, P.:  
1324 Future water resources for food production in five South Asian river basins and potential for adaptation –  
1325 A modeling study, *Sci. Total Environ.*, <https://doi.org/10.1016/j.scitotenv.2013.05.092>, 2013.  
1326
- 1327 Bollasina, M., Bertolani, L., and Tartari, G.: Meteorological observations at high altitude in the Khumbu Valley,  
1328 Nepal Himalayas, 1994–1999, *Bull. Glaciol. Res.*, 19, 1–11,  
1329 [https://www.seppyo.org/publication/bgr/archive/bgr\\_19\\_2002/attachment/bgr19p1/](https://www.seppyo.org/publication/bgr/archive/bgr_19_2002/attachment/bgr19p1/) (last access: 18 May  
1330 2026), 2002.  
1331
- 1332 Bonekamp, P. N. J., Wanders, N., Wiel, K., Lutz, A. F., and Immerzeel, W. W.: Using large ensemble modelling  
1333 to derive future changes in mountain specific climate indicators in a 2 and 3 °C warmer world in High  
1334 Mountain Asia, *Int. J. Climatol.*, 41, <https://doi.org/10.1002/joc.6742>, 2021.  
1335
- 1336 Bookhagen, B. and Burbank, D. W.: Topography, relief, and TRMM-derived rainfall variations along the  
1337 Himalaya, *Geophys. Res. Lett.*, 33, L08405, <https://doi.org/10.1029/2006GL026037>, 2006.  
1338
- 1339 Brock, B. W., Willis, I. C., and Sharp, M. J.: Measurement and parameterization of aerodynamic roughness length  
1340 variations at Haut Glacier d'Arolla, Switzerland, *J. Glaciol.*, 52, 281–297,  
1341 <https://doi.org/10.3189/172756506781828746>, 2006.  
1342
- 1343 Brun, F., King, O., Réveillet, M., Amory, C., Planchot, A., Berthier, E., Dehecq, A., Bolch, T., Fourteau, K.,  
1344 Brondex, J., Dumont, M., Mayer, C., Leinss, S., Hugonnet, R., and Wagnon, P.: Everest South Col Glacier  
1345 did not thin during the period 1984–2017, *The Cryosphere*, 17, 3251–3268, [https://doi.org/10.5194/tc-17-](https://doi.org/10.5194/tc-17-3251-2023)  
1346 3251-2023, 2023.  
1347
- 1348 Collins, M., Knutti, R., and Arblaster, J.: Long-term Climate Change: Projections, Commitments and  
1349 Irreversibility, in: *Climate Change 2013: The Physical Science Basis. Contribution of Working Group I to*  
1350 *the Fifth Assessment Report of the Intergovernmental Panel on Climate Change*, edited by: Stocker, T. F.,  
1351 Qin, D., Plattner, G.-K., Tignor, M., Allen, S. K., Boschung, J., Nauels, A., Xia, Y., Bex V., and Midgley,  
1352 P. M., Cambridge University Press, Cambridge, United Kingdom and New York, NY, USA, 1–108,  
1353 [https://www.ipcc.ch/site/assets/uploads/2018/02/WG1AR5\\_Chapter12\\_FINAL.pdf](https://www.ipcc.ch/site/assets/uploads/2018/02/WG1AR5_Chapter12_FINAL.pdf) (last access: 18 May  
1354 2026), 2013.  
1355

- 1356 Compagno, L., Huss, M., Miles, E. S., McCarthy, M. J., Zekollari, H., Dehecq, A., Pellicciotti, F., and Farinotti,  
1357 D.: Modelling supraglacial debris-cover evolution from the single-glacier to the regional scale: an  
1358 application to High Mountain Asia, *The Cryosphere*, 16, 1697–1718, [https://doi.org/10.5194/tc-16-1697-](https://doi.org/10.5194/tc-16-1697-2022)  
1359 2022, 2022.
- 1360
- 1361 Cuffey, K. M. and Paterson, W. S. B.: The physics of glaciers, 4th edn., Academic Press, 704 pp., ISBN-10: 0-  
1362 123694-61-2, ISBN-13: 978-0-123-69461-4, 2010.
- 1363
- 1364 Dehecq, A., Gourmelen, N., Gardner, A. S., Brun, F., Goldberg, D., Nienow, P. W., Berthier, E., Vincent, C.,  
1365 Wagnon, P., and Trouvé, E.: Twenty-first century glacier slowdown driven by mass loss in High Mountain  
1366 Asia, *Nat. Geosci.*, 12, 22–27, <https://doi.org/10.1038/s41561-018-0271-9>, 2019.
- 1367
- 1368 Egholm, D. L., Knudsen, M. F., Clark, C. D., and Lesemann, J. E.: Modeling the flow of glaciers in steep terrains:  
1369 The integrated second-order shallow ice approximation (iSOSIA), *J. Geophys. Res.*, 116,  
1370 <https://doi.org/10.1029/2010JF001900>, 2011.
- 1371
- 1372 Farinotti, D., Huss, M., Fürst, J. J., Landmann, J., Machguth, H., Maussion, F., and Pandit, A.: A consensus  
1373 estimate for the ice thickness distribution of all glaciers on Earth, *Nat. Geosci.*, 12, 168–173,  
1374 <https://doi.org/10.1038/s41561-019-0300-3>, 2019.
- 1375
- 1376 Farr, T. G., Rosen, P. A., Caro, E., Crippen, R., Duren, R., Hensley, S., Kobrick, M., Paller, M., Rodriguez, E.,  
1377 Roth, L., Seal, D., Shaffer, S., Shimada, J., Umland, J., Werner, M., Oskin, M., Burbank, D., and Alsdorf,  
1378 D.: The Shuttle Radar Topography Mission, *Rev. Geophys.*, 45, 2005RG000183,  
1379 <https://doi.org/10.1029/2005RG000183>, 2007.
- 1380
- 1381 Ferguson, J. C. and Vieli, A.: Modelling steady states and the transient response of debris-covered glaciers, *The*  
1382 *Cryosphere*, 15, 3377–3399, <https://doi.org/10.5194/tc-15-3377-2021>, 2021.
- 1383
- 1384 Förster, K., Hanzer, F., Winter, B., Marke, T., and Strasser, U.: An open-source MEteoroLOGical observation time  
1385 series DISaggregation Tool (MELODIST v0.1.1), *Geosci. Model Dev.*, 9, 2315–2333,  
1386 <https://doi.org/10.5194/gmd-9-2315-2016>, 2016.
- 1387
- 1388 Gades, A., Conway, H., Nereson, N., Naito, N., and Kadota, T.: Radio echo-sounding through supraglacial debris  
1389 on Lirung and Khumbu Glaciers, Nepal Himalayas, *Debris-Covered Glaciers (Proceedings of a workshop*  
1390 *held at Seattle, Washington, USA, September 2000)*, IAHS, 264, 13–22, ISBN-10: 1901502317, ISBN-13:  
1391 978-1901502312., 2000.
- 1392
- 1393 Gao, Y., Chen, F., Lettenmaier, D. P., Xu, J., Xiao, L., and Li, X.: Does elevation-dependent warming hold true  
1394 above 5000 m elevation? Lessons from the Tibetan Plateau, *npj Clim. Atmos. Sci.*, 1, 19,  
1395 <https://doi.org/10.1038/s41612-018-0030-z>, 2018.
- 1396
- 1397 Gromke, C., Manes, C., Walter, B., Lehning, M., and Guala, M.: Aerodynamic roughness length of fresh snow,  
1398 *Bound.-Lay. Meteorol.*, 141, 21–34, <https://doi.org/10.1007/s10546-011-9623-3>, 2011.
- 1399
- 1400 Guo, S., Chen, R., Liu, G., Han, C., Song, Y., Liu, J., Yang, Y., Liu, Z., Wang, X., Liu, X., and Wang, L.: Simple  
1401 parameterization of aerodynamic roughness lengths and the turbulent heat fluxes at the top of midlatitude  
1402 August-One Glacier, Qilian Mountains, China, *J. Geophys. Res.-Atmos.*, 123, 12066–12080,  
1403 <https://doi.org/10.1029/2018JD028875>, 2018.
- 1404
- 1405 Gupta, A. and Tarboton, D. G.: A tool for downscaling weather data from large-grid reanalysis products to finer  
1406 spatial scales for distributed hydrological applications, *Environ. Modell. Softw.*, 84, 50–69,  
1407 <https://doi.org/10.1016/j.envsoft.2016.06.014>, 2016.
- 1408
- 1409 Gutmann, E. D., Hamman, J. J., Clark, M. P., Eidhammer, T., Wood, A. W., and Arnold, J. R.: En-GARD: A  
1410 Statistical Downscaling Framework to Produce and Test Large Ensembles of Climate Projections, *J.*  
1411 *Hydrometeorol.*, 23, 1545–1561, <https://doi.org/10.1175/JHM-D-21-0142.1>, 2022.
- 1412
- 1413 Herreid, S. and Pellicciotti, F.: The state of rock debris covering Earth's glaciers, *Nat. Geosci.*, 13, 621–627,  
1414 <https://doi.org/10.1038/s41561-020-0615-0>, 2020.
- 1415

- 1416 Hornsey, J., Rowan, A. V., Kirkbride, M. P., Livingstone, S. J., Fabel, D., Rodes, A., Quincey, D. J., Hubbard, B.,  
1417 and Jomelli, V.: Be-10 Dating of Ice-Marginal Moraines in the Khumbu Valley, Nepal, Central Himalaya,  
1418 Reveals the Response of Monsoon-Influenced Glaciers to Holocene Climate Change, *J. Geophys. Res.-*  
1419 *Earth*, 127, <https://doi.org/10.1029/2022JF006645>, 2022.
- 1420
- 1421 Huintjes, E., Neckel, N., Hochschild, V., and Schneider, C.: Surface energy and mass balance at Purogangri ice  
1422 cap, central Tibetan Plateau, 2001–2011, *J. Glaciol.*, 61, 1048–1060,  
1423 <https://doi.org/10.3189/2015JoG15J056>, 2015.
- 1424
- 1425 Immerzeel, W. W., van Beek, L. P. H., Konz, M., Shrestha, A. B., and Bierkens, M. F. P.: Hydrological response  
1426 to climate change in a glacierized catchment in the Himalayas, *Climatic Change*, 110, 721–736,  
1427 <https://doi.org/10.1007/s10584-011-0143-4>, 2012.
- 1428
- 1429 Immerzeel, W., Petersen, L., Ragettli, S., and Pellicciotti, F.: The importance of observed gradients of air  
1430 temperature and precipitation for modeling runoff from a glacierized watershed in the Nepalese Himalayas,  
1431 *Water Resour. Res.*, 50, 2212–2226, <https://doi.org/10.1002/2013WR014506>, 2014.
- 1432
- 1433 Irvine-Fynn, T. D., Sanz-Ablanedo, E., Rutter, N., Smith, M. W., and Chandler, J. H.: Measuring glacier surface  
1434 roughness using plot-scale, close-range digital photogrammetry, *J. Glaciol.*, 60, 957–969,  
1435 <https://doi.org/10.3189/2014JoG14J032>, 2014.
- 1436
- 1437 Jennings, K. S., Winchell, T. S., Livneh, B., and Molotch, N. P.: Spatial variation of the rain–snow temperature  
1438 threshold across the Northern Hemisphere, *Nat. Commun.*, 9, 1148, [https://doi.org/10.1038/s41467-018-  
1439 \*03629-7\*, 2018.](https://doi.org/10.1038/s41467-018-03629-7)
- 1440
- 1441 Jouvét, G., Huss, M., Funk, M., and Blatter, H.: Modelling the retreat of Grosser Aletschgletscher, Switzerland,  
1442 in a changing climate, *J. Glaciol.*, 57, 1033–1045, <https://doi.org/10.3189/002214311798843359>, 2011.
- 1443
- 1444 Kaini, S., Nepal, S., Pradhananga, S., Gardner, T., and Sharma, A. K.: Representative general circulation models  
1445 selection and downscaling of climate data for the transboundary Koshi river basin in China and Nepal, *Int.*  
1446 *J. Climatol.*, 40, 4131–4149, <https://doi.org/10.1002/joc.6447>, 2019.
- 1447
- 1448 Katzenberger, A., Schewe, J., Pongratz, J., and Levermann, A.: Robust increase of Indian monsoon rainfall and  
1449 its variability under future warming in CMIP6 models, *Earth Syst. Dynam.*, 12, 367–386,  
1450 <https://doi.org/10.5194/esd-12-367-2021>, 2021.
- 1451
- 1452 Khadka, A., Matthews, T., Perry, L. B., Koch, I., Wagon, P., Shrestha, D., Sherpa, T. C., Aryal, D., Tait, A.,  
1453 Sherpa, T. G., Tuladhar, S., Baidya, S. K., Elvin, S., Elmore, A. C., Gajurel, A., and Mayewski, P. A.:  
1454 Weather On Mount Everest During The 2019 Summer Monsoon, *Weather*, 76, 205–207,  
1455 <https://doi.org/10.1002/wea.3931>, 2021.
- 1456
- 1457 King, O., Bhattacharya, A., Ghuffar, S., Tait, A., Guilford, S., Elmore, A. C., and Bolch, T.: Six Decades of Glacier  
1458 Mass Changes around Mt. Everest Are Revealed by Historical and Contemporary Images, *One Earth*, 3,  
1459 608–620, <https://doi.org/10.1016/j.oneear.2020.10.019>, 2020.
- 1460
- 1461 Knap, W. H. and Oerlemans, J.: The surface albedo of the Greenland ice sheet: satellite-derived and in situ  
1462 measurements in the Søndre Strømfjord area during the 1991 melt season, *J. Glaciol.*, 42, 364–374,  
1463 <https://doi.org/10.3189/S0022143000004214>, 1996.
- 1464
- 1465 Kneib, M., Maussion, F., Brun, F., Carcanade, G., Farinotti, D., Huss, M., Van Tiel, M., Jouberton, A., Schmitt,  
1466 P., Schuster, L., Dehecq, A., and Champollion, N.: Topographically-controlled contribution of avalanches  
1467 to glacier mass balance in the 21st century, *Nat. Commun.*, 16, 10122, [https://doi.org/10.1038/s41467-025-  
1468 \*65608-z\*, 2025.](https://doi.org/10.1038/s41467-025-65608-z)
- 1469
- 1470 Kraaijenbrink, P. D. A., Bierkens, M. F. P., Lutz, A. F., and Immerzeel, W. W.: Impact of a global temperature rise  
1471 of 1.5 degrees Celsius on Asia's glaciers, *Nature*, 549, 257–260, <https://doi.org/10.1038/nature23878>, 2017.
- 1472
- 1473 Lafon, T., Dadson, S., Buys, G., and Prudhomme, C.: Bias correction of daily precipitation simulated by a regional  
1474 climate model: a comparison of methods, *Int. J. Climatol.*, 33, 1367–1381, 2013.
- 1475

- 1476 Laha, S., Kumari, R., Singh, S., Mishra, A., Sharma, T., Banerjee, A., Nainwal, H. C., and Shankar, R.: Evaluating  
1477 the contribution of avalanching to the mass balance of Himalayan glaciers, *Ann. Glaciol.*, 58, 110–118,  
1478 <https://doi.org/10.1017/aog.2017.27>, 2017.  
1479
- 1480 Lente, G. and Ósz, K.: Barometric formulas: various derivations and comparisons to environmentally relevant  
1481 observations, *ChemTexts*, 6, 1–14, <https://doi.org/10.1007/s40828-020-0111-6>, 2020.  
1482
- 1483 Li, H., Sheffield, J., and Wood, E. F.: Bias correction of monthly precipitation and temperature fields from  
1484 Intergovernmental Panel on Climate Change AR4 models using equidistant quantile matching, *J. Geophys.*  
1485 *Res.-Atmos.*, 115, <https://doi.org/10.1029/2009JD012882>, 2010.  
1486
- 1487 Luo, M., Liu, T., Meng, F., Duan, Y., Frankl, A., Bao, A., and De Maeyer, P.: Comparing bias correction methods  
1488 used in downscaling precipitation and temperature from regional climate models: A case study from the  
1489 Kaidu River basin in western China, *Water*, 10, 1046, <https://doi.org/10.3390/w10081046>, 2018.  
1490
- 1491 Lutz, A. F., Immerzeel, W. W., Kraaijenbrink, P. D., Shrestha, A. B., and Bierkens, M. F.: Climate change impacts  
1492 on the upper Indus hydrology: sources, shifts and extremes, *PloS One*, 11, e0165630,  
1493 <https://doi.org/10.1371/journal.pone.0165630>, 2016.  
1494
- 1495 Marzeion, B., Hock, R., Anderson, B., Bliss, A., Champollion, N., Fujita, K., Huss, M., Immerzeel, W. W.,  
1496 Kraaijenbrink, P., Malles, J., Maussion, F., Radić, V., Rounce, D. R., Sakai, A., Shannon, S., Van De Wal,  
1497 R., and Zekollari, H.: Partitioning the Uncertainty of Ensemble Projections of Global Glacier Mass Change,  
1498 *Earth's Future*, 8, e2019EF001470, <https://doi.org/10.1029/2019EF001470>, 2020.  
1499
- 1500 Matthews, T., Perry, L. B., Koch, I., Aryal, D., Khadka, A., Shrestha, D., Abernathy, K., Elmore, A. C., Seimon,  
1501 A., Tait, A., Elvin, S., Tuladhar, S., Baidya, S. K., Potocki, M., Birkel, S. D., Kang, S., Sherpa, T. C.,  
1502 Gajurel, A., and Mayewski, P. A.: Going to Extremes: Installing the World's Highest Weather Stations on  
1503 Mount Everest, *B. Am. Meteorol. Soc.*, 101, E1870–E1890, <https://doi.org/10.1175/BAMS-D-19-0198.1>,  
1504 2020.  
1505
- 1506 Maurer, J. M., Schaefer, J. M., Rupper, S., and Corley, A.: Acceleration of ice loss across the Himalayas over the  
1507 past 40 years, *Sci. Adv.*, 5, eaav7266, <https://doi.org/10.1126/sciadv.aav7266>, 2019.  
1508
- 1509 Miles, E. S., Willis, I., Buri, P., Steiner, J. F., Arnold, N. S., and Pellicciotti, F.: Surface Pond Energy Absorption  
1510 Across Four Himalayan Glaciers Accounts for 1/8 of Total Catchment Ice Loss, *Geophys. Res. Lett.*, 45,  
1511 <https://doi.org/10.1029/2018GL079678>, 2018a.  
1512
- 1513 Miles, K. E., Hubbard, B., Quincey, D. J., Miles, E. S., Sherpa, T. C., Rowan, A. V., and Doyle, S. H.: Polythermal  
1514 structure of a Himalayan debris-covered glacier revealed by borehole thermometry, *Sci. Rep.*, 8, 16825,  
1515 <https://doi.org/10.1038/s41598-018-34327-5>, 2018b.  
1516
- 1517 Miles, K. E., Hubbard, B., Miles, E. S., Quincey, D. J., Rowan, A. V., Kirkbride, M., and Hornsey, J.: Continuous  
1518 borehole optical televueing reveals variable englacial debris concentrations at Khumbu Glacier, Nepal,  
1519 *Commun. Earth Environ.*, 2, 12, <https://doi.org/10.1038/s43247-020-00070-x>, 2021.  
1520
- 1521 Miles, K. E., Hubbard, B., Miles, E. S., Quincey, D. J., and Rowan, A. V.: Internal structure of a Himalayan debris-  
1522 covered glacier revealed by borehole optical televueing, *J. Glaciol.*, 69, 811–822,  
1523 <https://doi.org/10.1017/jog.2022.100>, 2022.  
1524
- 1525 Mölg, T., Maussion, F., Yang, W., and Scherer, D.: The footprint of Asian monsoon dynamics in the mass and  
1526 energy balance of a Tibetan glacier, *The Cryosphere*, 6, 1445–1461, [https://doi.org/10.5194/tc-6-1445-](https://doi.org/10.5194/tc-6-1445-2012)  
1527 2012, 2012.  
1528
- 1529 Mölg, T., Maussion, F., and Scherer, D.: Mid-latitude westerlies as a driver of glacier variability in monsoonal  
1530 High Asia, *Nat. Clim. Change*, 4, 68–73, <https://doi.org/10.1038/nclimate2055>, 2014.  
1531
- 1532 Mott, R., Stiperski, I., and Nicholson, L.: Spatio-temporal flow variations driving heat exchange processes at a  
1533 mountain glacier, *The Cryosphere*, 14, 4699–4718, <https://doi.org/10.5194/tc-14-4699-2020>, 2020.  
1534

- 1535 Nakawo, M.: Processes Which Distribute Supraglacial Debris On The Khumbu Glacier, Nepal Himalaya, *Ann.*  
1536 *Glaciol.*, 8, <https://doi.org/10.3189/S0260305500001294>, 1986.  
1537
- 1538 Nicholson, L., Wirbel, A., Mayer, C., and Lambrecht, A.: The Challenge of Non-Stationary Feedbacks in  
1539 Modeling the Response of Debris-Covered Glaciers to Climate Forcing, *Front. Earth Sci.*, 9, 662695,  
1540 <https://doi.org/10.3389/feart.2021.662695>, 2021.  
1541
- 1542 Oerlemans, J.: *Glaciers and climate change*, CRC Press, eBook ISBN 9781003760672, 2001.  
1543
- 1544 Oulkar, S. N., Peacey, M. W., Mitrev, M., Quincey, D. J., Hubbard, B., Matthews, T., Oulkar, A. S., Miles, K. E.,  
1545 and Rowan, A. V.: Design and implementation of a robust data logging and satellite telemetry system for  
1546 remote cryospheric research, *Geosci. Instrum. Method. Data Syst.*, 15, 75–88, <https://doi.org/10.5194/gi-15-75-2026>, 2026.  
1547
- 1548
- 1549 Owen, L. A., Robinson, R., Benn, D. I., Finkel, R. C., Davis, N. K., Yi, C., Putkonen, J., Li, D., and Murray, A.  
1550 S.: Quaternary glaciation of Mount Everest, *Quaternary Sci. Rev.*, 28, 1412–1433,  
1551 <https://doi.org/10.1016/j.quascirev.2009.02.010>, 2009.  
1552
- 1553 Pedersen, J. S. T., Van Vuuren, D. P., Aparicio, B. A., Swart, R., Gupta, J., and Santos, F. D.: Variability in historical  
1554 emissions trends suggests a need for a wide range of global scenarios and regional analyses, *Commun.*  
1555 *Earth Environ.*, 1, 41, <https://doi.org/10.1038/s43247-020-00045-y>, 2020.  
1556
- 1557 Pellicciotti, F., Stephan, C., Miles, E., Herreid, S., Immerzeel, W. W., and Bolch, T.: Mass-balance changes of the  
1558 debris-covered glaciers in the Langtang Himal, Nepal, from 1974 to 1999, *J. Glaciol.*, 61, 373–386,  
1559 <https://doi.org/10.3189/2015JoG13J237>, 2015.  
1560
- 1561 Pepin, N. C., Arnone, E., Gobiet, A., Haslinger, K., Kotlarski, S., Notarnicola, C., Palazzi, E., Seibert, P., Serafin,  
1562 S., Schöner, W., Terzago, S., Thornton, J. M., Vuille, M., and Adler, C.: Climate Changes and Their  
1563 Elevational Patterns in the Mountains of the World, *Rev. Geophys.*, 60,  
1564 <https://doi.org/10.1029/2020RG000730>, 2022.  
1565
- 1566 Piani, C., Weedon, G. P., Best, M., Gomes, S. M., Viterbo, P., Hagemann, S., and Haerter, J. O.: Statistical bias  
1567 correction of global simulated daily precipitation and temperature for the application of hydrological  
1568 models, *J. Hydrol.*, 395, 199–215, <https://doi.org/10.1016/j.jhydrol.2010.10.024>, 2010.  
1569
- 1570 Pierce, D. W., Barnett, T. P., Santer, B. D., and Gleckler, P. J.: Selecting global climate models for regional climate  
1571 change studies, *P. Natl. Acad. Sci. USA*, 106, 8441–8446, <https://doi.org/10.1073/pnas.0900094106>, 2009.  
1572
- 1573 Potocki, M., Mayewski, P. A., Matthews, T., Perry, L. B., Schwikowski, M., Tait, A. M., Korotkikh, E., Clifford,  
1574 H., Kang, S., Sherpa, T. C., Singh, P. K., Koch, I., and Birkel, S.: Mt. Everest's highest glacier is a sentinel  
1575 for accelerating ice loss, *npj Clim. Atmos. Sci.*, 5, 7, <https://doi.org/10.1038/s41612-022-00230-0>, 2022.  
1576
- 1577 Pritchard, H. D.: Asia's shrinking glaciers protect large populations from drought stress, *Nature*, 569, 649–654,  
1578 <https://doi.org/10.1038/s41586-019-1240-1>, 2019.  
1579
- 1580 Purdie, H., Kerr, T., Robson, B., Anderson, B., Lorrey, A. M., Rack, W., Brasington, J., and Bealing, P.: Mass  
1581 balance characteristics of the “vanishing” Rolleston Glacier, New Zealand, *Ann. Glaciol.*, 66, e31,  
1582 <https://doi.org/10.1017/aog.2025.10032>, 2025.  
1583
- 1584 Quincey, D. J., Luckman, A., and Benn, D.: Quantification of Everest region glacier velocities between 1992 and  
1585 2002, using satellite radar interferometry and feature tracking, *J. Glaciol.*, 55, 596–606,  
1586 <https://doi.org/10.3189/002214309789470987>, 2009.  
1587
- 1588 Ragettli, S., Immerzeel, W. W., and Pellicciotti, F.: Contrasting climate change impact on river flows from high-  
1589 altitude catchments in the Himalayan and Andes Mountains, *P. Natl. Acad. Sci. USA*, 113, 9222–9227,  
1590 <https://doi.org/10.1073/pnas.1606526113>, 2016.  
1591
- 1592 Reiter, P., Gutjahr, O., Schefczyk, L., Heinemann, G., and Casper, M.: Does applying quantile mapping to  
1593 subsamples improve the bias correction of daily precipitation?, *Int. J. Climatol.*, 38, 1623–1633, 2018.  
1594

- 1595 RGI 7.0 Consortium: A Dataset of Global Glacier Outlines, Version 7.0. Boulder, Colorado USA. NSIDC:  
1596 National Snow and Ice Data Center [data set], <https://doi.org/10.5067/f6jmovy5navz>, 2023.  
1597
- 1598 Roering, J. J., Kirchner, J. W., and Dietrich, W. E.: Evidence for nonlinear, diffusive sediment transport on  
1599 hillslopes and implications for landscape morphology, *Water Resour. Res.*, 35, 853–870,  
1600 <https://doi.org/10.1029/1998WR900090>, 1999.  
1601
- 1602 Rounce, D. R., Hock, R., Maussion, F., Hugonnet, R., Kochtitzky, W., Huss, M., Berthier, E., Brinkerhoff, D.,  
1603 Compagno, L., Copland, L., Farinotti, D., Menounos, B., and McNabb, R. W.: Global glacier change in  
1604 the 21st century: Every increase in temperature matters, *Science*, 379, 78–83,  
1605 <https://doi.org/10.1126/science.abo1324>, 2023.  
1606
- 1607 Rowan, A. V.: The “Little Ice Age” in the Himalaya: A review of glacier advance driven by Northern Hemisphere  
1608 temperature change, *The Holocene*, 27, 292–308, <https://doi.org/10.1177/0959683616658530>, 2017.  
1609
- 1610 Rowan, A. and Pedersen, V. K.: annrowan/isosia: iSOSIA version used in Schlich-Davies et al. (spm-3.3.3r),  
1611 Zenodo [code], <https://doi.org/10.5281/zenodo.12666864>, 2024.  
1612
- 1613 Rowan, A. V., Egholm, D. L., Quincey, D. J., and Glasser, N. F.: Modelling the feedbacks between mass balance,  
1614 ice flow and debris transport to predict the response to climate change of debris-covered glaciers in the  
1615 Himalaya, *Earth Planet. Sc. Lett.*, 430, 427–438, <https://doi.org/10.1016/j.epsl.2015.09.004>, 2015.  
1616
- 1617 Rowan, A. V., Egholm, D. L., Quincey, D. J., Hubbard, B., King, O., Miles, E. S., Miles, K. E., and Hornsey, J.:  
1618 The Role of Differential Ablation and Dynamic Detachment in Driving Accelerating Mass Loss From a  
1619 Debris-Covered Himalayan Glacier, *J. Geophys. Res.-Earth*, 126, <https://doi.org/10.1029/2020JF005761>,  
1620 2021.  
1621
- 1622 Ruane, A. C., Goldberg, R., and Chryssanthacopoulos, J.: Climate forcing datasets for agricultural modeling:  
1623 Merged products for gap-filling and historical climate series estimation, *Agr. Forest Meteorol.*, 200, 233–  
1624 248, <https://doi.org/10.1016/j.agrformet.2014.09.016>, 2015.  
1625
- 1626 Salerno, F., Guyennon, N., Thakuri, S., Viviano, G., Romano, E., Vuillermoz, E., Cristofanelli, P., Stocchi, P.,  
1627 Agrillo, G., Ma, Y., and Tartari, G.: Weak precipitation, warm winters and springs impact glaciers of south  
1628 slopes of Mt. Everest (central Himalaya) in the last 2 decades (1994–2013), *The Cryosphere*, 9, 1229–  
1629 1247, <https://doi.org/10.5194/tc-9-1229-2015>, 2015.  
1630
- 1631 Salerno, F., Guyennon, N., Yang, K., Shaw, T. E., Lin, C., Colombo, N., Romano, E., Gruber, S., Bolch, T.,  
1632 Alessandri, A., Cristofanelli, P., Putero, D., Diolaiuti, G., Tartari, G., Verza, G., Thakuri, S., Balsamo, G.,  
1633 Miles, E. S., and Pellicciotti, F.: Local cooling and drying induced by Himalayan glaciers under global  
1634 warming, *Nat. Geosci.*, 16, 1120–1127, <https://doi.org/10.1038/s41561-023-01331-y>, 2023.  
1635
- 1636 Sanjay, J., Krishnan, R., Shrestha, A. B., Rajbhandari, R., and Ren, G.-Y.: Downscaled climate change projections  
1637 for the Hindu Kush Himalayan region using CORDEX South Asia regional climate models, *Advances in*  
1638 *Climate Change Research*, 8, 185–198, <https://doi.org/10.1016/j.accre.2017.08.003>, 2017.  
1639
- 1640 Sauter, T., Arndt, A., and Schneider, C.: COSIPY v1.3 – an open-source coupled snowpack and ice surface energy  
1641 and mass balance model, *Geosci. Model Dev.*, 13, 5645–5662, <https://doi.org/10.5194/gmd-13-5645-2020>,  
1642 2020.  
1643
- 1644 Shaw, T. E., Miles, E. S., Chen, D., Jouberton, A., Kneib, M., Fugger, S., Ou, T., Lai, H.-W., Fujita, K., Yang, W.,  
1645 Fatichi, S., and Pellicciotti, F.: Multi-decadal monsoon characteristics and glacier response in High  
1646 Mountain Asia, *Environ. Res. Lett.*, 17, 104001, <https://doi.org/10.1088/1748-9326/ac9008>, 2022.  
1647
- 1648 Shaw, T. E., Buri, P., McCarthy, M., Miles, E. S., and Pellicciotti, F.: Local Controls on Near-Surface Glacier  
1649 Cooling Under Warm Atmospheric Conditions, *J. Geophys. Res.-Atmos.*, 129, e2023JD040214,  
1650 <https://doi.org/10.1029/2023JD040214>, 2024.  
1651
- 1652 Shaw, T. E., Miles, E. S., McCarthy, M., Buri, P., Guyennon, N., Salerno, F., Carturan, L., Brock, B., and  
1653 Pellicciotti, F.: Mountain glaciers recouple to atmospheric warming over the twenty-first century, *Nat.*  
1654 *Clim. Change*, 15, 1212–1218, <https://doi.org/10.1038/s41558-025-02449-0>, 2025.

- 1655  
1656  
1657  
1658  
1659  
1660  
1661  
1662  
1663  
1664  
1665  
1666  
1667  
1668  
1669  
1670  
1671  
1672  
1673  
1674  
1675  
1676  
1677  
1678  
1679  
1680  
1681  
1682  
1683  
1684  
1685  
1686  
1687  
1688  
1689  
1690  
1691  
1692  
1693  
1694  
1695  
1696  
1697  
1698  
1699  
1700  
1701  
1702  
1703
- Shea, J. M., Immerzeel, W. W., Wagnon, P., Vincent, C., and Bajracharya, S.: Modelling glacier change in the Everest region, Nepal Himalaya, *The Cryosphere*, 9, 1105–1128, <https://doi.org/10.5194/tc-9-1105-2015>, 2015.
- Sherpa, S. F., Wagnon, P., Brun, F., Berthier, E., Vincent, C., Lejeune, Y., Arnaud, Y., Kayastha, R. B., and Sinisalo, A.: Contrasted surface mass balances of debris-free glaciers observed between the southern and the inner parts of the Everest region (2007–15), *J. Glaciol.*, 63, 637–651, <https://doi.org/10.1017/jog.2017.30>, 2017.
- Strickland, R. M., Covington, M. D., Gulley, J. D., Kayastha, R. B., and Blackstock, J. M.: Englacial Drainage Drives Positive Feedback Depression Growth on the Debris-Covered Ngozumpa Glacier, Nepal, *Geophys. Res. Lett.*, 50, e2023GL104389, <https://doi.org/10.1029/2023GL104389>, 2023.
- Sun, W., Qin, X., Wang, Y., Chen, J., Wentao, D., Tong, Z., and Huai, B.: The response of surface mass and energy balance of a continental glacier to climate variability, western Qilian Mountains, China, *Clim. Dynam.*, 50, 3557–3570, <https://doi.org/10.1007/s00382-017-3823-6>, 2018.
- Ueno, K., Toyotsu, K., Bertolani, L., and Tartari, G.: Stepwise Onset of Monsoon Weather Observed in the Nepal Himalaya, *Mon. Weather Rev.*, 136, 2507–2522, <https://doi.org/10.1175/2007MWR2298.1>, 2008.
- Vacco, D. A., Alley, R. B., and Pollard, D.: Glacial advance and stagnation caused by rock avalanches, *Earth Planet. Sc. Lett.*, 294, 123–130, <https://doi.org/10.1016/j.epsl.2010.03.019>, 2010.
- Vrac, M., Stein, M. L., Hayhoe, K., and Liang, X. Z.: A general method for validating statistical downscaling methods under future climate change, *Geophys. Res. Lett.*, 34, <https://doi.org/10.1029/2007GL030295>, 2007.
- Wagnon, P., Lafaysse, M., Lejeune, Y., Maisincho, L., Rojas, M., and Chazarin, J. P.: Understanding and modeling the physical processes that govern the melting of snow cover in a tropical mountain environment in Ecuador, *J. Geophys. Res.-Atmos.*, 114, <https://doi.org/10.1029/2009JD012292>, 2009.
- Watson, C. S., Quincey, D. J., Smith, M. W., Carrivick, J. L., Rowan, A. V., and James, M. R.: Quantifying ice cliff evolution with multi-temporal point clouds on the debris-covered Khumbu Glacier, Nepal, *J. Glaciol.*, 63, 823–837, <https://doi.org/10.1017/jog.2017.47>, 2017.
- Wirbel, A., Jarosch, A. H., and Nicholson, L.: Modelling debris transport within glaciers by advection in a full-Stokes ice flow model, *The Cryosphere*, 12, 189–204, <https://doi.org/10.5194/tc-12-189-2018>, 2018.
- Wohlfahrt, G., Hammerle, A., Haslwanter, A., Bahn, M., Tappeiner, U., and Cernusca, A.: Disentangling leaf area and environmental effects on the response of the Net Ecosystem CO<sub>2</sub> Exchange to diffuse radiation, *Geophys. Res. Lett.*, 35, <https://doi.org/10.1029/2008gl035090>, 2008.
- Wohlfahrt, G., Hammerle, A., Niedrist, G., Scholz, K., Tomelleri, E., and Zhao, P.: On the energy balance closure and net radiation in complex terrain, *Agr. Forest Meteorol.*, 226–227, 37–49, <https://doi.org/10.1016/j.agrformet.2016.05.012>, 2016.
- Yang, K., Guyennon, N., Ouyang, L., Tian, L., Tartari, G., and Salerno, F.: Impact of summer monsoon on the elevation-dependence of meteorological variables in the south of Central Himalaya, *Int. J. Climatol.*, 38, 1748–1759, <https://doi.org/10.1002/joc.5293>, 2017.